

# **MSc Computational Sciences: Introduction to Computational Meteorology**

Aiko Voigt

November 5, 2024

# Table of contents

<b>Preface</b>	<b>3</b>
<b>1 Logistics</b>	<b>4</b>
1.1 Lecture plan for part 1 . . . . .	5
1.2 Learning objectives for part 1 . . . . .	6
<b>2 Atmospheric thermodynamics</b>	<b>7</b>
2.1 Vertical structure of the atmosphere . . . . .	7
2.2 Atmospheric composition . . . . .	10
2.3 Ideal gas law of dry air . . . . .	11
2.4 Moist air . . . . .	12
2.5 Important moisture variables . . . . .	13
2.6 Clausius-Clapeyron relation . . . . .	13
2.7 Ideal gas law for moist air . . . . .	15
2.8 Hydrostatic balance for moist air . . . . .	15
2.9 First law of thermodynamics for non-saturated air . . . . .	15
2.10 Special cases of the first law . . . . .	16
2.11 The many forms of atmospheric temperatures . . . . .	16
2.12 Potential temperature . . . . .	16
2.13 Equivalent potential temperature . . . . .	17
2.14 Dew-point temperature . . . . .	18
2.15 Lapse rates . . . . .	18
2.16 Dry lapse rate . . . . .	18
2.17 Moist lapse rate . . . . .	19
2.18 Skew T - ln p diagram . . . . .	19
<b>3 Atmospheric convection</b>	<b>22</b>
3.1 Buoyancy . . . . .	22
3.2 Local instability . . . . .	23
3.3 Potential instability . . . . .	26
3.4 CIN and CAPE . . . . .	29
3.5 Km-scale simulations to compute convection explicitly . . . . .	30
3.6 What is the fundamental modeling problem in representing convection and turbulence? . . . . .	30
3.7 Parametrizations of subgrid-scale processes . . . . .	37

3.8	Representing convection in atmospheric models . . . . .	40
3.8.1	Hard convective adjustment . . . . .	40
3.8.2	Mass-flux schemes . . . . .	44
3.8.3	Superparametrization . . . . .	45
3.8.4	Machine learning . . . . .	50
3.8.5	Km-scale models . . . . .	50
<b>4</b>	<b>Interlude: challenges for global km-scale modeling</b>	<b>52</b>
4.1	The data avalanche . . . . .	52
4.2	Can km-scale models simulate enough days per wall-clock day to be useful? . . . . .	53
<b>5</b>	<b>Atmospheric radiation</b>	<b>57</b>
5.1	Planck's law . . . . .	57
5.2	Spectral complexity . . . . .	57
5.3	The atmospheric energy budget and global-mean precipitation . . . . .	60
5.4	The interplay of radiation and convection in setting the temperature profile of the atmosphere . . . . .	66
5.5	Representation of radiation in climate and weather models . . . . .	69
	<b>References</b>	<b>73</b>

# Preface

The lecture script is in the form of a [Quarto book](#).

# 1 Logistics

- Lectures: Wednesday, 14:30-16:00 (90 mins), UZA II 2G542 (“Wetterbesprechungsraum”)
- Associated exercises: 262004 UE, Aiko Voigt, first meeting on 8.10.2024 at 10am s.t. in UZA II 2F513, participation in first meeting is mandatory

Dates for oral exams:

- 29.1. 14:30-16:00 (UZA II, 2G552)
- 26.2. 14:30-16:00 (UZA II, 2G552)
- additional dates will be communicated later

For questions regarding the content of the lectures please use the Moodle forum. For personal matters you can approach us in person or contact us by email.

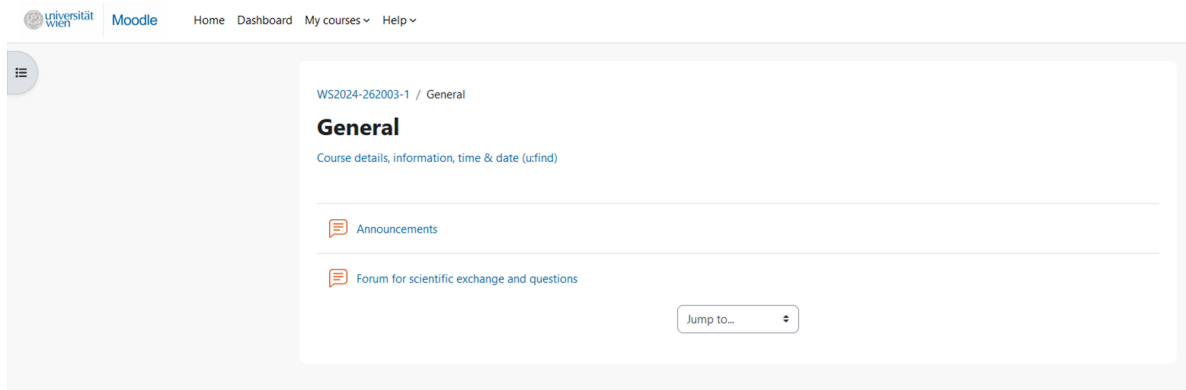
A screenshot of a Moodle General forum page. At the top, there is a navigation bar with the University of Vienna logo, "Moodle", "Home", "Dashboard", "My courses", and "Help". The main title is "WS2024-262003-1 / General". Below the title, the word "General" is bolded. There is a link to "Course details, information, time & date (urfind)". Below this, there are two sections: "Announcements" and "Forum for scientific exchange and questions". A "Jump to..." dropdown menu is visible at the bottom right of the forum area.

Figure 1.1: Moodle Forum

## Winter semester 2024/25

Beginning of semester and classes	1 October 2024
No classes	2 November 2024
Christmas break	18 December 2024 to 6 January 2025
End of classes	31 January 2025
Lecture-free period (semester break)	1 to 28 February 2025
End of semester	28 February 2025

Figure 1.2: Academic calendar of Uni Wien for W2024

- Nationalfeiertag: Samstag, 26. Oktober 2024
- Allerheiligen: Freitag, 1. November 2024
- Mariä Empfängnis: Sonntag, 8. Dezember 2024
- Christtag: Mittwoch, 25. Dezember 2024
- Stefanitag: Donnerstag, 26. Dezember 2024

### Feiertage im Jahr 2025

- Neujahr: Mittwoch, 1. Jänner 2025
- Heilige Drei Könige: Montag, 6. Jänner 2025

Figure 1.3: Public holidays during W2024

## 1.1 Lecture plan for part 1

Date	Lecture	note
02.10.2024	L1	Logistics
09.10.2024	L2	
16.10.2024	L3	
23.10.2024	L4	
30.10.2024	L5	
06.11.2024	L6	
13.11.2024		reserve date

Lectures 1 - 6 form part 1 of the course . Lectures 7 and following will be held by Martin Weissmann, starting on 20.11.2024.

## **1.2 Learning objectives for part 1**

- You will develop an understanding of atmospheric thermodynamics, convection and radiation. These processes are fundamental to the vertical exchange of energy and the vertical structure of the troposphere.
- We will discuss how these processes are represented in numerical models of climate and weather.
- Another goal is to show how your skills in physics, mathematics, or data science can be applied to the field of climate and weather research.

## 2 Atmospheric thermodynamics

This chapter provides a quick introduction to the thermodynamics of the atmosphere. A solid understanding of the latter will lay the foundation to understand how convection and radiation interact to set the vertical structure of the troposphere. Indeed, the simplest useful model of the troposphere is radiative-convective equilibrium: heating by convection and condensation of water vapor is balanced by radiative cooling (Figure 2.1). On the one hand convective instability tightly couples tropospheric and surface temperatures, on the other hand radiative cooling of the atmosphere necessitates vertical energy transport by convective motions. Suki Manabe was fundamental to the development of this class of models in the 1960s and used it as the basis for global climate models, which won him the Nobel Prize in Physics in 2021.

### 2.1 Vertical structure of the atmosphere

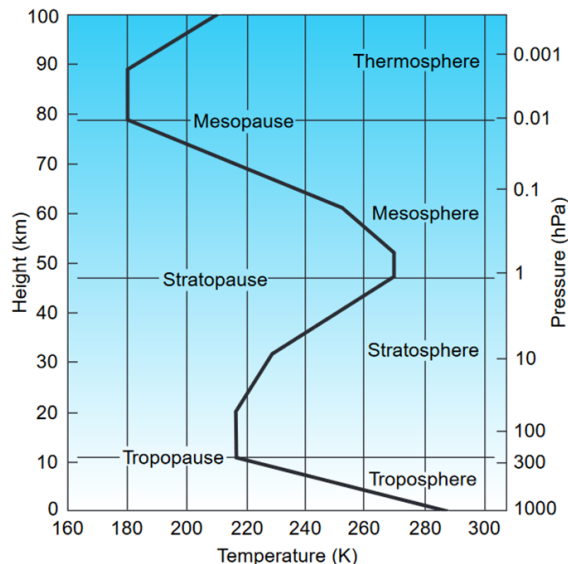


**Fig. 1.9** A typical midlatitude vertical temperature profile, as represented by the U.S. Standard Atmosphere.

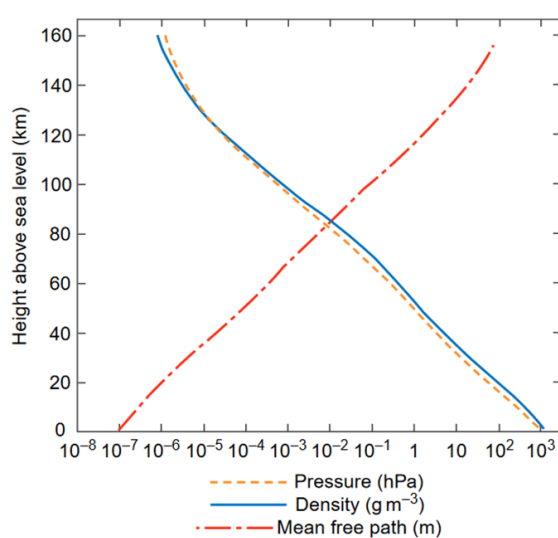


**Fig. 1.8** Vertical profiles of pressure in units of hPa, density in units of  $\text{kg m}^{-3}$ , and mean free path (in meters) for the U.S. Standard Atmosphere.

Figure 2.2: Figs. 1.8 and 1.9 of Wallace and Hobbs (2006).

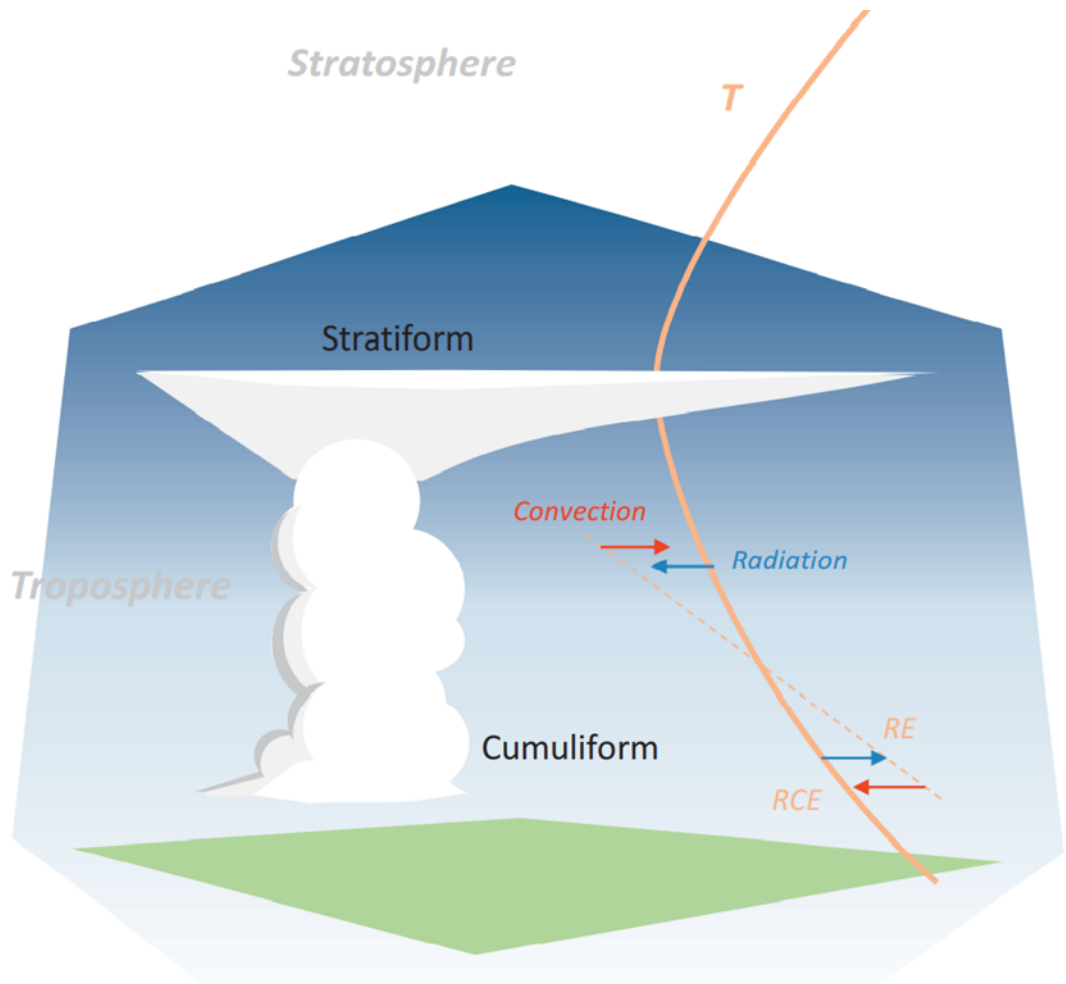


Figure 2.1: Vertical structure of tropospheric temperatures as a result of radiation and convection. Fig. 5.11 of Siebesma et al. (2020).

At around 100 km, the mean free path becomes large enough so that the gas constituents are now longer well mixed by turbulence and collisions and become independent of each other. This height is the top of the homosphere. Above it, the volume mixing ratios of the atmospheric gases change due to gravitational force and the lighter molecules H and He become predominant while heavier molecules such as N<sub>2</sub> and O<sub>2</sub> are prevented from reaching higher altitudes.

The right figure also illustrates the hydrostatic balance:  $\frac{dp}{dz} = -\rho \cdot g$ , where  $p$  is air pressure,  $z$  is height,  $\rho = 9.81 \text{ m s}^{-1}$  is air density and  $g$  is the gravitational acceleration.

## 2.2 Atmospheric composition

**Table 1.1** Fractional concentrations by volume of the major gaseous constituents of the Earth's atmosphere up to an altitude of 105 km, with respect to dry air

Constituent <sup>a</sup>	Molecular weight	Fractional concentration by volume
Nitrogen (N <sub>2</sub> )	28.013	78.08%
Oxygen (O <sub>2</sub> )	32.000	20.95%
Argon (Ar)	39.95	0.93%
<b>Water vapor (H<sub>2</sub>O)</b>	18.02	0–5%
<b>Carbon dioxide (CO<sub>2</sub>)</b>	44.01	380 ppm
Neon (Ne)	20.18	18 ppm
Helium (He)	4.00	5 ppm
<b>Methane (CH<sub>4</sub>)</b>	16.04	1.75 ppm
Krypton (Kr)	83.80	1 ppm
Hydrogen (H <sub>2</sub> )	2.02	0.5 ppm
<b>Nitrous oxide (N<sub>2</sub>O)</b>	56.03	0.3 ppm
<b>Ozone (O<sub>3</sub>)</b>	48.00	0–0.1 ppm

<sup>a</sup> So called *greenhouse gases* are indicated by bold-faced type. For more detailed information on minor constituents, see Table 5.1.

Figure 2.3: Tab. 1.1 of Wallace and Hobbs (2006).

Air consists of a mixture of gases:

- “permanent” gases: N<sub>2</sub>, O<sub>2</sub> and inert (noble) gases Ar, Ne, He, Kr

- variable components: H<sub>2</sub>O, CO<sub>2</sub>, CH<sub>4</sub>, N<sub>2</sub>O, O<sub>3</sub>

The variable components can undergo phase changes (H<sub>2</sub>O) and chemical reactions (e.g., O<sub>3</sub> chemistry). But the permanent gases are well mixed within the lowest 100 km, i.e., the homosphere. Therefore, we can define a gas constant  $R_d$  for dry air for the mixture of “permanent” gases.

## 2.3 Ideal gas law of dry air

Dry air is a mixture of  $k$  gases. The ideal gas law for dry air is

$$p = \rho R_d T,$$

where  $p$  is pressure,  $\rho$  is density,  $R_d = 287 \text{ J/kgK}$  is the gas constant for dry air, and  $T$  is the temperature of the air.

The derivation is as follows. We start from the general form of the ideal gas law:

$$pV = nR^*T, \quad (2.1)$$

where  $p$  is pressure,  $V$  volume,  $n$  is the number of molecules in mol,  $R^*=8.314 \text{ J/Kmol}$  is the *universal* gas constant, and  $T$  is temperature of the gas.

For a mixture of  $n$  gases, the number of molecules is

$$n = \sum_{i=1}^k n_i$$

and the total mass is

$$M = \sum_{i=1}^k n_i m_i,$$

where  $m_i$  is the molar mass in kg/mol of the individual components of the mixture.

Multiplying the universal gas law with  $M$  yields

$$\frac{pV}{M} = \underbrace{\frac{n}{M}}_{R_d} R^* T,$$

which is the ideal gas law of dry air provided that we define the dry air gas constant  $R_d$  according to the gas composition in the well-mixed homosphere.

Side remark: Remember that Avogadro's constant  $N_A = 6.22 \cdot 10^{23}$  gives numbers of molecules per mol.

## 2.4 Moist air

For a mixture of dry air and water vapor, the total pressure  $p$  is given by

$$p = p_d + e.$$

$p_d = \rho_d R_d T$  and  $e = \rho_v R_v T$  are the partial pressures of dry air and water vapor, respectively.  $\rho_v$  is the water vapor density,  $R_v = 461 J/kgK$  is the gas constant for water vapor.

This yields the ideal gas law for moist air:

$$p = \rho R_d T_v.$$

$\rho = \rho_d + \rho_v$  is the density of the dry air-vapor mixture,  $T_v$  is the virtual temperature.

Derivation:

$$p = p_d + e \tag{2.2}$$

$$= (\rho_d R_d + \rho_v R_v) T \tag{2.3}$$

$$= \underbrace{\rho R_d \left( \frac{\rho_d}{\rho} + \frac{\rho_v}{\rho} \frac{R_v}{R_d} \right) T}_{T_v} \tag{2.4}$$

The virtual temperature is the temperature that a dry parcel of air would need to have to match the density of the moist parcel, at a given pressure.  $T_v \geq T$  because  $R_v > R_d$ .  $T_v = T$  for  $\rho_v = 0$ .

As a result, for the same pressure and temperature moist air is lighter than dry air.

This can be seen as follows. At a given pressure  $p$  and temperature  $T$ , the density of a dry parcel is  $\rho_d = \frac{p}{R_d T}$ , and the density of a moist parcel is  $\rho = \frac{p}{R_d T_v} \leq \rho_d$  is obviously smaller because  $T_v \geq T$ . One can also understand this from the fact that water vapor molecules are lighter than the N<sub>2</sub> and O<sub>2</sub> molecules that make up most of dry air.

## 2.5 Important moisture variables

- water vapor mixing ratio in  $g/kg$ :  $w = \frac{\rho_v}{\rho_d}$
- specific humidity in  $g/kg$ :  $q = \frac{\rho_v}{\rho}$
- relative humidity in fraction or per cent:  $RH = \frac{e}{e_s}$
- saturation vapor pressure in Pa:  $e_s$
- $e_s$  is given by given by the Clausius Clapeyron equation

## 2.6 Clausius-Clapeyron relation

$$\frac{de_s}{dT} = \frac{L_v e_s}{R_v T^2}$$

$L_v$  is the latent heat of condensation,  $L_v \approx 2500 \text{ kJ/kg}$  (at  $T = 0 \text{ deg C}$ ).

$L_v$  decreases slightly with increasing temperature: due to thermal motions, water molecules in the liquid phase already possess some of the energy required to overcome the attraction to neighboring molecules (see, e.g., chapter 7.2, page 177 of G. W. Petty (2008)).

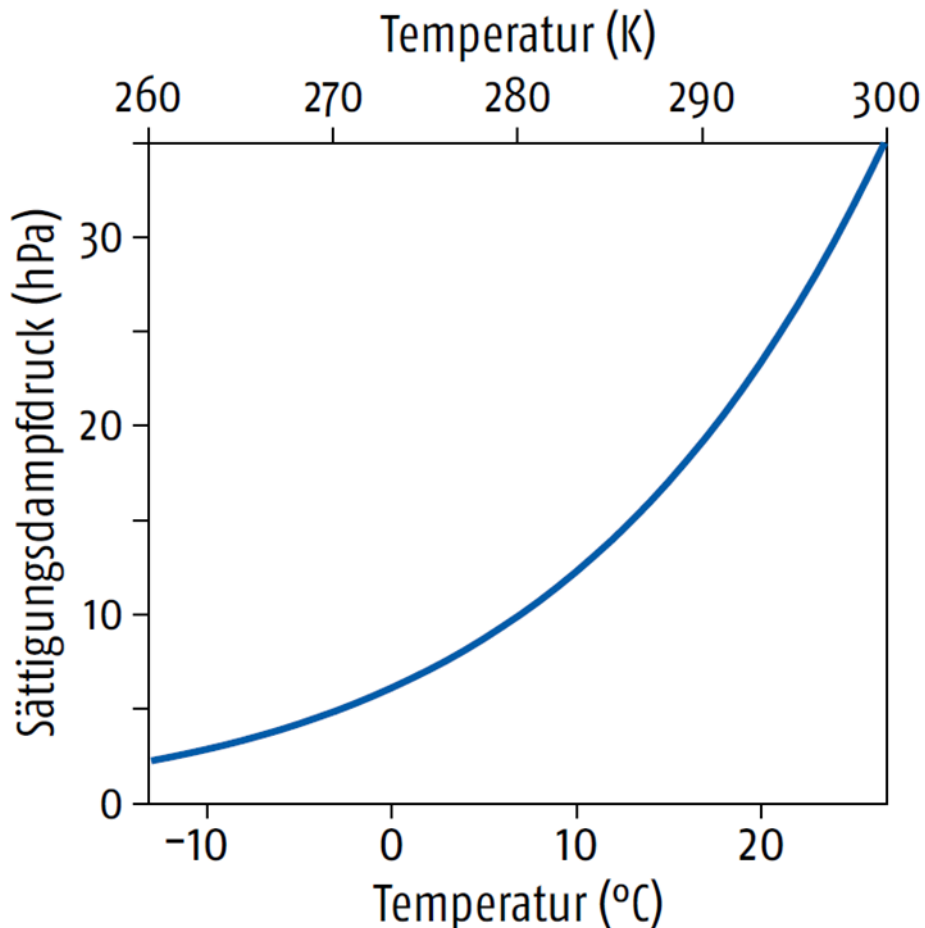


Figure 2.4: Saturation vapor pressure  $e_s$  as given by the Clausius-Clapeyron relation as a function of temperature. Fig. 2.14 of Brönnimann (2018)

The Clausius-Clapeyron relation states that the saturation vapor pressure increases by about 7% for every 1K increase in temperature. The saturation specific humidity also increases with 7%/K. This means that warm air can “hold” more water vapor than cold air, which is important, for example, for changing extreme precipitation events as a result of global warming. The increase of 7%/K implies a doubling for a 10K temperature increase, an effect known as “compound interest effect” in finance.

## 2.7 Ideal gas law for moist air

$$p = \rho R_d \underbrace{(1 + (1/\epsilon - 1)q)}_{T_v} T,$$

with  $\epsilon = \frac{R_d}{R_v} = 0.622$  and hence  $T_v \approx (1 + 0.61q)T$ , which again shows that the virtual temperature is higher than the actual temperature

## 2.8 Hydrostatic balance for moist air

$$\frac{\partial p}{\partial z} = -\rho g = -\frac{pg}{R_d T_v}.$$

## 2.9 First law of thermodynamics for non-saturated air

$$\delta q = du + pd\alpha$$

$\delta q$  is the heat transferred to/from the environment,  $du$  is the change in internal energy of the air parcel, and  $pd\alpha$  is the pressure-volume work.  $\alpha = 1/\rho$  is the specific volume.

$du = c_v dT$ ,  $c_v$  is the specific heat capacity at constant volume. For the atmosphere  $c_v = \frac{5}{2}R$  because dry air is mostly a diatomic gas and hence  $c_v = 718 J/kgK$ .

$$\delta q = c_v dT + pd\alpha \quad (2.5)$$

$$\delta q = c_p dT - \alpha dp \quad (2.6)$$

$$(2.7)$$

$c_p = c_v + R$  is the specific heat capacity at constant pressure.

To show the second version, use the equation of state:

$$d(p\alpha) = \alpha dp + pd\alpha = RdT \quad (2.8)$$

$$pd\alpha = RdT - \alpha dp. \quad (2.9)$$

$$(2.10)$$

Hence,

$$\delta q = c_v dT + p d\alpha \quad (2.11)$$

$$= c_v dT + R dT - \alpha dp \quad (2.12)$$

$$= c_p dT - \alpha dp \quad (2.13)$$

$$(2.14)$$

## 2.10 Special cases of the first law

- Isobaric process:  $dp = 0 \rightarrow \delta q = c_p dT = \left(\frac{c_p}{c_v}\right) c_v dT = \left(\frac{c_p}{c_v}\right) c_v du$
- Isochoric process:  $d\alpha = 0 \rightarrow \delta q = c_v dT = du$
- Adiabatic process:  $\delta q = 0 \rightarrow c_v dT = -p d\alpha, c_p dT = \alpha dp$

Adiabatic processes are of special significance in meteorology because many of the changes that affect a moving volume of air in the atmosphere can be approximated as adiabatic. See chapter 5.8 of G. W. Petty (2008).

Isobaric and isochoric processes are important for the coupling of the fluid-dynamical solver of climate and weather models (“dynamical core”) to the subgrid-scale parametrizations (“physics”). For example, the ICON climate and weather model uses isochoric coupling because the model is based on height coordinates. See chapter 3.7.2 of the [2019 ICON model tutorial](#).

## 2.11 The many forms of atmospheric temperatures

### 2.12 Potential temperature

$$\theta = T \left( \frac{1000 \text{ hPa}}{p} \right)^\kappa$$

An important property of  $\theta$  is that it is conserved under dry adiabatic processes, where dry here means that no water vapor phase changes take place (i.e., no condensation, evaporation).  $\theta$  is hence a conserved quantity under the condition of dry adiabatic changes, such as the lifting of a clear-air air parcel.

The derivation of  $\theta$  is as follows. Start from the first law for adiabatic processes and use  $p\alpha = RT$ :

$$c_p dT = \alpha dp = \frac{RT}{p} dp,$$

Divide through  $c_p$  and T:

$$\frac{1}{T}dT = \frac{R}{c_p} \frac{1}{p} dp$$

Integrate from a point with  $(T_0, p_0)$  to another point  $(T, p)$ :

$$\int_{T_0}^T \frac{1}{T'} dT' = \frac{R}{c_p} \int_{p_0}^p \frac{1}{p'} dp, \quad (2.15)$$

$$\ln\left(\frac{T}{T_0}\right) = \frac{R}{c_p} \ln\left(\frac{p}{p_0}\right). \quad (2.16)$$

(2.17)

Use  $a \ln b = \ln(b^a)$  to arrive at the Poisson equation:

$$\frac{T}{T_0} = \left(\frac{p}{p_0}\right)^\kappa.$$

$\kappa = R/c_p$ , hence for dry air  $\kappa = R_d/c_p \approx 0.286$ . Note that for moist air  $\kappa$  has a slightly different value because  $R \neq R_d$ .

This then allows us to define the potential temperature  $\theta$  as the temperature  $T_0$  at a reference pressure level  $p_0$ . Typically,  $p_0 = 1000 \text{ hPa}$  is chosen.

## 2.13 Equivalent potential temperature

The equivalent potential temperature  $\theta_e$  is conserved for dry *and* moist adiabatic motions.

$$\begin{aligned} \theta_e &= \theta \exp\left(\frac{L_v q_s}{c_p T}\right) && \text{for saturated air parcels} \\ \theta_e &= \theta \exp\left(\frac{L_v q}{c_p T_{LCL}}\right) && \text{for non-saturated air parcels} \end{aligned}$$

$T_{LCL}$  in the equation for non-saturated air parcels is the temperature for which saturation would occur if the parcel was lifted adiabatically.  $T_{LCL}$  is the temperature of the lifting condensation level. Obviously,  $T_{LCL} \leq T$ .

$T_{LCL}$  is related to the dew-point temperature  $T_d$  but differs from it because the former involves adiabatic lifting whereas the latter is calculated at the original pressure location of the air parcel without adiabatic lifting.

For a full derivation see chapter 2.5.9 of Lohmann, Lüönd, and Mahrt (2016), equations 2.95-2.100. Here, it may suffice to say that the derivation starts from the first law of thermodynamics, now allowing for water vapor phase changes and using  $\delta q = 0$ :

$$\delta q = c_p dT - \alpha dp + L_v dq_s,$$

where  $q_s = q_s(T, p)$  is the saturation specific humidity.

## 2.14 Dew-point temperature

The dew-point temperature  $T_d$  is the temperature to which an air parcel would need to cool to reach a relative humidity of 100% while staying at the same pressure.

$T_d$  is a measure of the vapor content. If  $T_d$  is only slightly lower than  $T$ , the parcel contains is relatively moist; if  $T_d$  is much smaller than  $T$  the parcel is relatively dry.

## 2.15 Lapse rates

### 2.16 Dry lapse rate

$$\Gamma_d = -\frac{dT}{dz} = \frac{g}{c_p} \approx 10 \text{ K/km}$$

Derivation: start from first law for dry adiabatic processes and combine it with the hydrostatic balance.

$$\begin{aligned}\delta q &= c_p dT - \alpha dp = 0 \\ \frac{\partial p}{\partial z} &= -\rho/g \\ c_p dT - \alpha dp &= 0 \\ c_p dT + \underbrace{\alpha \rho g}_{1} dz &= 0 \\ \frac{dT}{dz} &= -\frac{g}{c_p} = -\Gamma_d\end{aligned}$$

## 2.17 Moist lapse rate

$$\Gamma_m = \left[ 1 + \frac{L_v dq_s}{c_p dT} \right]^{-1} \quad \Gamma_d < \Gamma_d$$

The moist lapse rate is always smaller than the dry lapse rate, and equals the dry lapse rate when the air parcel is not saturated. In contrast to the dry lapse rate, the moist lapse rate depends on temperature.

In the upper troposphere and above, where temperatures are -40 deg C and lower,  $q_s$  becomes so small that the moist lapse rate is very close to the dry lapse rate.

The temperature dependence arises because the saturation specific humidity  $q_s$  depends on temperature via the Clausius-Clapeyron equation, which states that  $q_s$  increases essentially exponentially with temperature.

The derivation starts from first law for moist adiabatic processes and proceed analogously to the derivation of dry lapse rate. The full derivation can be found in Lohmann, Lüönd, and Mahrt (2016).

## 2.18 Skew T - ln p diagram

Skew T - ln p diagrams as shown in Figure 2.5 illustrate the vertical structure of temperature and moisture, and hence provide information on stability and the possibility of convection.

Skew T - ln p diagrams contain the following lines:

- isobars are horizontal,
- isotherms are lines at a 45 deg angle (thus the “skew-T” part of the name),
- saturated pseudo-adiabatic ascents along the moist adiabat, shown by the grey short dashed lines,
- dry adiabats shown in grey solid lines,
- lines with constant water vapor mixing ratio  $w$  in  $g/kg$ , shown by long grey dashes,
- the temperature of the environmental air  $T_{env}$ , shown in red,
- the dew point temperature of the environmental air  $T_{d,env}$ , shown in blue.

The example shown here is the 3 July 2009 sounding from Cabauw in the Netherlands, prior to a period of severe weather. One can see a well-mixed boundary clear-air layer between the surface and around 900hPa, with temperatures following the dry adiabat. At around 900 and 700hPa, the air is just short of saturation, as  $T_d$  is only slightly smaller than  $T$ , but no condensation has occurred and no clouds have formed. Further above, in the mid-troposphere,  $T_d$  is much smaller than  $T$ , indicating low relative humidity.

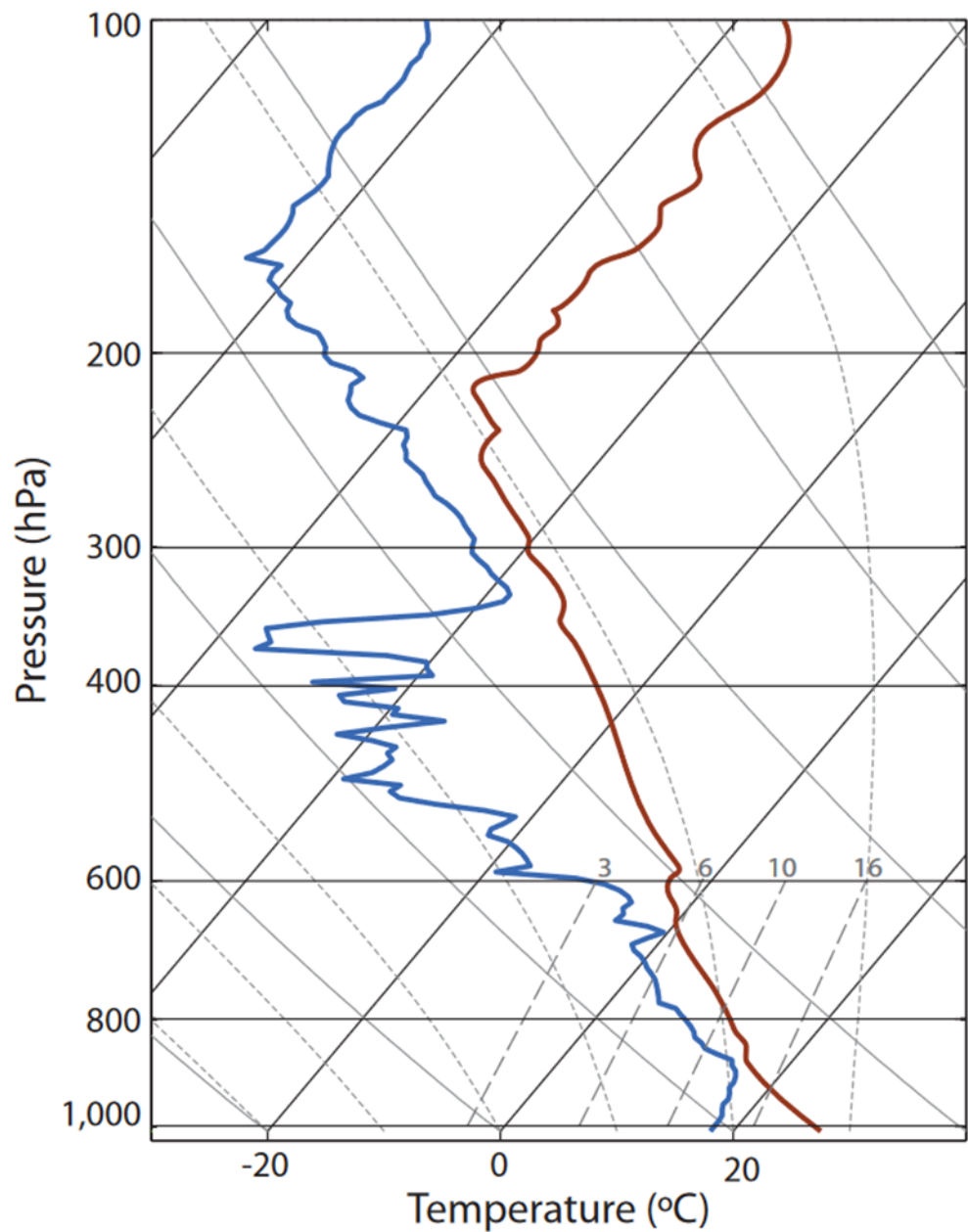


Figure 2.5: Fig. 2.3 of Siebesma et al. (2020)

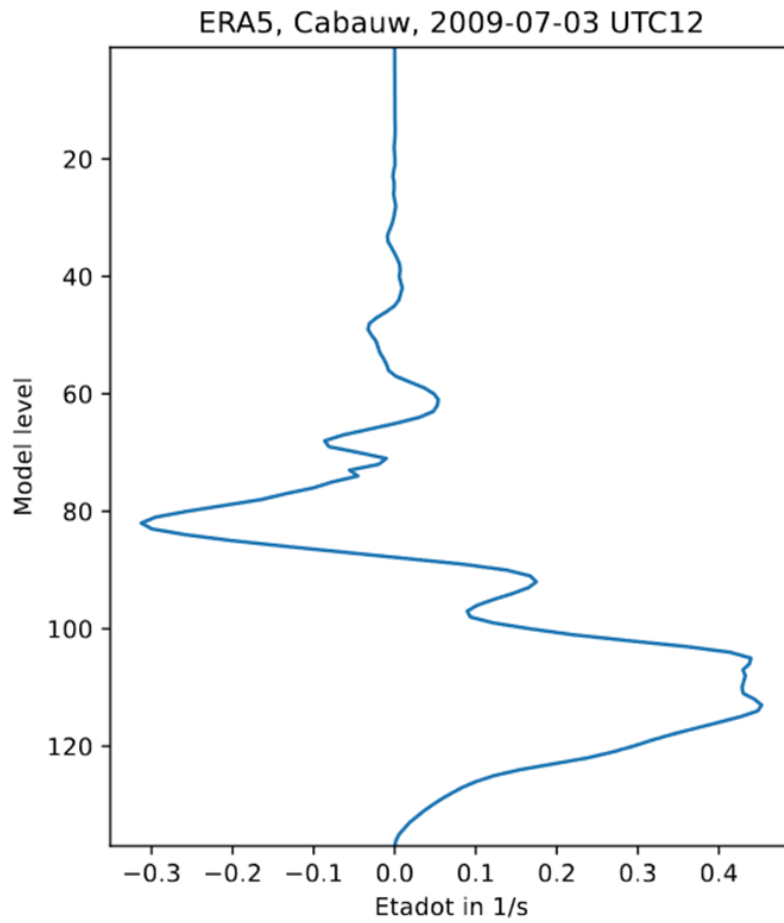


Figure 2.6: ERA5 reanalysis, model level 137: surface, 100: 500hPa, 80: 250hPa, 60: 100hPa.

The temperature and humidity structure are related to vertical motion: according to the ERA5 reanalysis and consistent with expectations, the mid-troposphere was experiencing descent, leading to adiabatic warming and low relative humidity there. Eta is proportional to pressure, which means that etadot is proportional to the pressure velocity, with negative values indicating ascent (towards decreasing pressure) and positive values indicating descent (towards increasing pressure). For details on eta ( $\eta$ ), see the Sect.2.1 of the [IFS model documentation Part III](#).

# 3 Atmospheric convection

This chapter discusses the phenomenon of atmospheric convection, which is the vertical movement of air caused by differences in temperature and moisture. Convection plays a crucial role in redistributing energy vertically within the atmosphere, and is central to phenomena like thunderstorms, cloud formation, and circulations.

## 3.1 Buoyancy

To derive the buoyancy  $b$  of an air parcel compared to its environment, we make use of Archimedes principle

$$b = - \left[ \frac{\rho - \rho_{env}}{\rho} \right] g,$$

where  $\rho$  is the density of the air parcel and  $\rho_{env}$  is the density of the environmental (surrounding) air. By means of the ideal gas law  $\rho = \frac{p}{R_d T_v}$  and  $\rho_{env} = \frac{p}{R_d T_{v,env}}$ , we can write the buoyancy as a function of the virtual temperatures of the air parcel,  $T_v$ , and its environment,  $T_{v,env}$ .

$$\begin{aligned} b &= - \left[ \frac{\rho - \rho_{env}}{\rho} \right] g \\ &= - \left[ \frac{\frac{1}{T_v} - \frac{1}{T_{v,env}}}{\frac{1}{T_v}} \right] g \\ &= - \left[ \frac{T_{v,env} - T_v}{T_v T_{v,env}} \right] g \\ &= \left[ \frac{T_v - T_{v,env}}{T_{v,env}} \right] g, \end{aligned}$$

where from the 2nd to 3rd line we have multiplied the nominator and denominator by  $T_v T_{v,env}$ .

Thus, the buoyancy is given by the virtual temperature difference divided by the virtual temperature of the environment:

$$b = \left[ \frac{T_v - T_{v,env}}{T_{v,env}} \right] g.$$

This is nothing more than the well known fact that warm air is lighter and rises due to positive buoyancy. Note here that we have neglected the effect of condensate loading, which decreases buoyancy.

## 3.2 Local instability

Local instability refers to a condition where a small parcel of air, when displaced vertically by an infinitesimal amount, becomes buoyant and continues to rise or fall on its own. This is illustrated in Figure 3.1. To read the figure, recall that buoyancy, in terms of density, is given by  $b = -\left[\frac{\rho - \rho_{env}}{\rho}\right]g \propto -\delta\rho$ .

- Case (a): The air is unsaturated, hence we consider dry adiabatic displacements. If the air parcel is displaced upward, it has negative buoyancy  $b < 0$  because its density is higher than that of the surrounding air. Likewise, if the air parcel is displaced downward, it gains positive buoyancy  $b > 0$ . This is a stable situation, as the air parcel will oscillate and ultimately return to its original position.
- Case (b): As in case a, the air is unsaturated and we need to consider dry adiabatic displacements. Now, however, environmental density decreases less strongly with height, and the air parcel experiences  $b > 0$  when displaced upward and  $b < 0$  when displaced downward. The situation is hence unstable. Because density is inversely proportional to temperature, case b differs from case a by a stronger decrease of environmental temperature with height (i.e., a stronger environmental lapse rate).
- Case (c): The air is saturated and we need to consider moist adiabatic displacements. In contrast to case a, the weaker change of the parcel temperature with height means that the situation is unstable: the parcel experience positive buoyancy when displaced upward and negative buoyancy when displaced downward. The comparison of cases a and c illustrates how moisture affects stability and convection.

The regions of atmospheric stability are illustrated in Figure 3.2.

- absolute instability:  $\frac{\partial T}{\partial z} < \Gamma_d$ ,  $\frac{\partial \Theta}{\partial z} < 0$
- conditional instability:  $\Gamma_d < \frac{\partial T}{\partial z} < \Gamma_m$
- absolute stability:  $\frac{\partial T}{\partial z} > \Gamma_m$

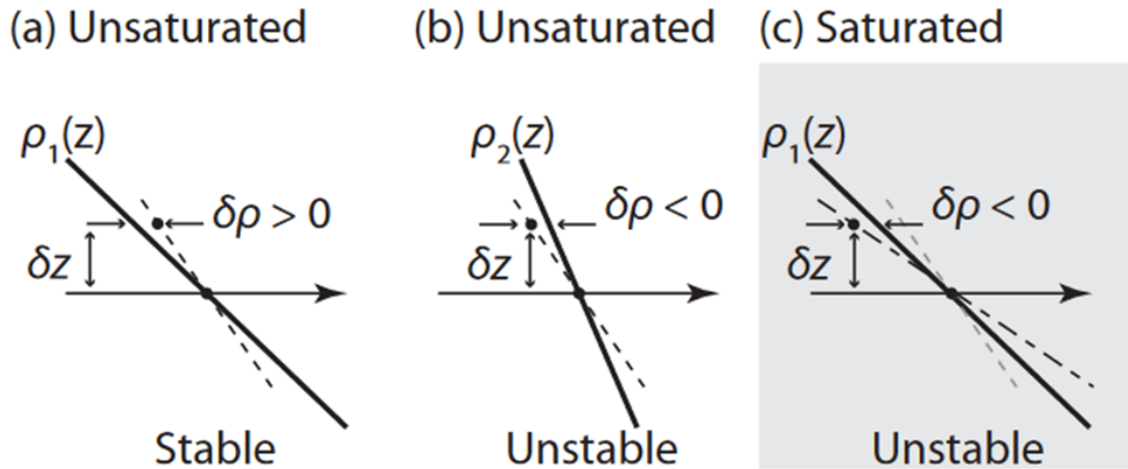


**FIGURE 2.5:** Schematic showing how buoyancy changes for an infinitesimal isentropic displacement  $\delta$  of a fluid parcel relative to the environmental density profile  $\rho(z)$  within the layer and denoted by the solid line. Panels (a) and (c) share the same density stratification,  $\rho_1(z)$ , but the fluid in (c) is saturated. Panels (a) and (b) both show an unsaturated case, but  $\rho_2(z)$  in panel (b) decreases less strongly in height than  $\rho_1(z)$  in panel (a). Lines also denote unsaturated (dashed) and saturated (dashed and dotted) isentropic density change with height.

Figure 3.1: Fig. 2.5 of Siebesma et al. (2020). The solid line gives the environmental density, the dashed line the density of the air parcel when displaced vertically following the dry adiabat (a, b) and the moist adiabat (c).

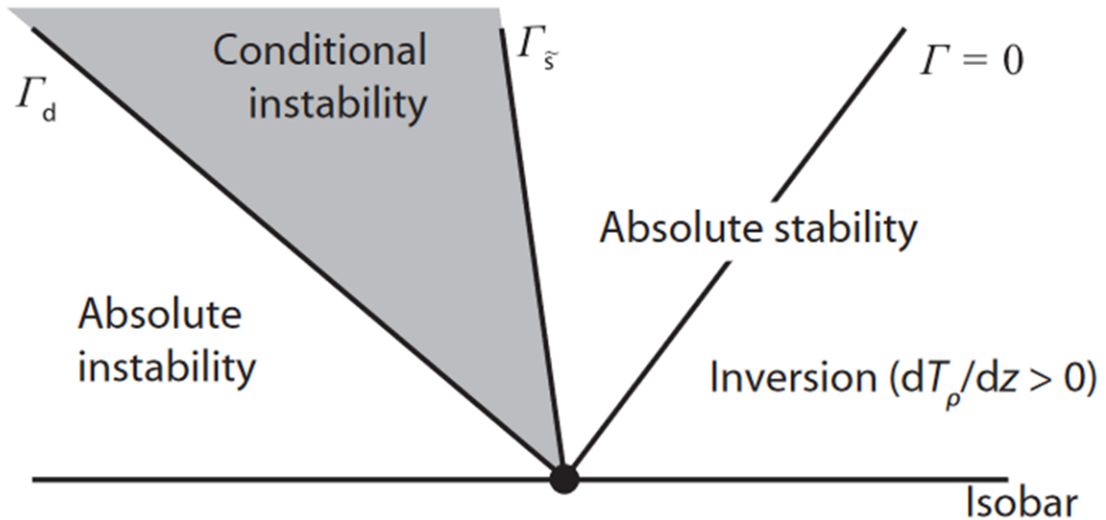


**FIGURE 2.6:** Different regions of atmospheric stability, as delineated by the fundamental lines demarcating different lapse rates on a skew- $T$  diagram.

Figure 3.2: Fig. 2.6 of Siebesma et al. (2020).  $\Gamma_{\tilde{s}}$  is the moist adiabat  $\Gamma_m$ . The vertical axis is proportional to height and pressure, with height increasing towards the top of the figure and pressure decreasing.

### 3.3 Potential instability

A different kind of vertical instability is potential instability, which is also referred to as convective instability. The stability of a layer of air can change if the entire layer is lifted over some distance, instead of an infinitesimal displacement of an air parcel. The lifting of a layer of moist air can transform an initially stable air mass into an unstable or conditionally unstable state. The presence of a potential instability can then lead to vigorous convection and thunderstorms.

The lifting of an entire layer that is needed to trigger potential instability can happen when an air mass is forced to rise owing to orography, due to frontal lifting (synoptic scales up to about 1000 km), or due to a cold pool density current (mesoscales up to 100 km).

Cold pools are small-scale areas of downdraft air that are cooled due to evaporation of rain and spread on the surface underneath precipitating clouds (Figure 3.3). The passage of a cold pool front is generally associated with a rapid decrease in air temperature, a fast increase in air pressure and a considerable pick-up of wind speed. Since lifting at the cold pool edge often triggers new convection, they are key for understanding the organization of convective precipitation. Since lifting at the cold pool edge often triggers new convection, they are key for understanding the organization of convective precipitation. High-resolution simulations with horizontal grid spacing below 1 km explicitly resolve small-scale phenomena such as cold pools. For more information on cold pools, see <https://fesstval.de/en/campaign/cold-pools>.

The video below illustrates cold pools. It shows a large-eddy simulation with horizontal grid spacing of about 100m for a situation with several deep convective events. Below the clouds, the vertical velocity ( $w$ ) field at 200m illustrates the large structures of downward and horizontally spreading motions near the surface below deep raining clouds. Red means upward motion, blue means downward motion. The simulation was performed using a GPU-resident LES simulation (GALES) with CUDA technology at TU Delft in 2011(!).

<https://www.youtube.com/watch?v=HTMsWDQwubA>

Potential instability can occur for moist air but not for dry air. Whether there is potential instability depends on the vertical distribution of humidity in the atmosphere. This is illustrated in Figure 3.4 and discussed for three cases in the following. All cases consider a layer of air between 1000 and 900hPa that is stable with respect to infinitesimal displacements of air parcels. Yet, when the layer is lifted to between 700 and 600hPa, it becomes unstable in one of the cases.

- Stable case (left in Figure 3.4): The specific humidity is higher in the upper than the lower part of the layer, as can be deduced from the wet bulb potential temperature  $\Theta_w$ . The lower part of the layer of air at 1000hPa lifts along the dry adiabat up to 900hPa and then along the moist adiabat up to 700hPa. The upper part at 900hPa is already saturated and is lifted along the moist adiabat up to 600hPa. After having been lifted, the temperature within the layer air is given by the thick vertical line in the skew T - ln

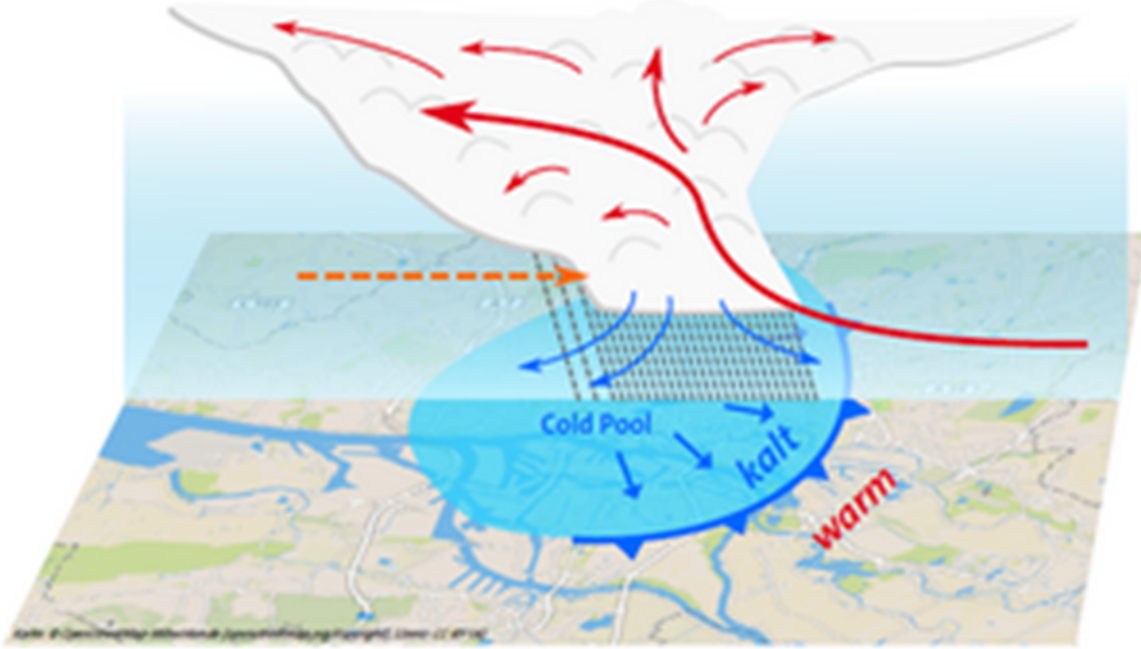


Figure 3.3: A schematic illustration of cold pools. Figure from <https://fesstval.de/fesstheme-2020/fessth-cold-pool>.

$p$  diagram, which implies absolutely stable conditions (see Figure 3.2). Thus, the layer is still stably stratified after having been lifted.

- Neutral case (middle in Figure 3.4): both the upper and lower parts first follow the dry adiabat when being lifted, and then follow the moist adiabat. After having been lifted to 700-600hPa, the temperature within the layer is exactly on the moist adiabat, and so the layer is neutral stratified with respect to moist adiabatic displacements of air parcels.
- Unstable case (right in Figure 3.4): The specific humidity is higher in the lower than the upper part of the layer. That is, moister air underlies drier air - a situation prone to potential instability. When being lifted, the lower part of the layer switches from the dry to the moist adiabat faster than the upper part. As a result, after the lifting the temperature within the layer decreases with height faster than the dry adiabat and the layer has become unstable.

The key differences between the three cases is the moisture content of the lower part of the layer relative to the upper part. In the stable case, the lower part is drier than the upper part. But in the unstable case, the lower part is closer to saturation than the upper part. Thus, potential instability can occur when relatively moist air is below relatively dry air.

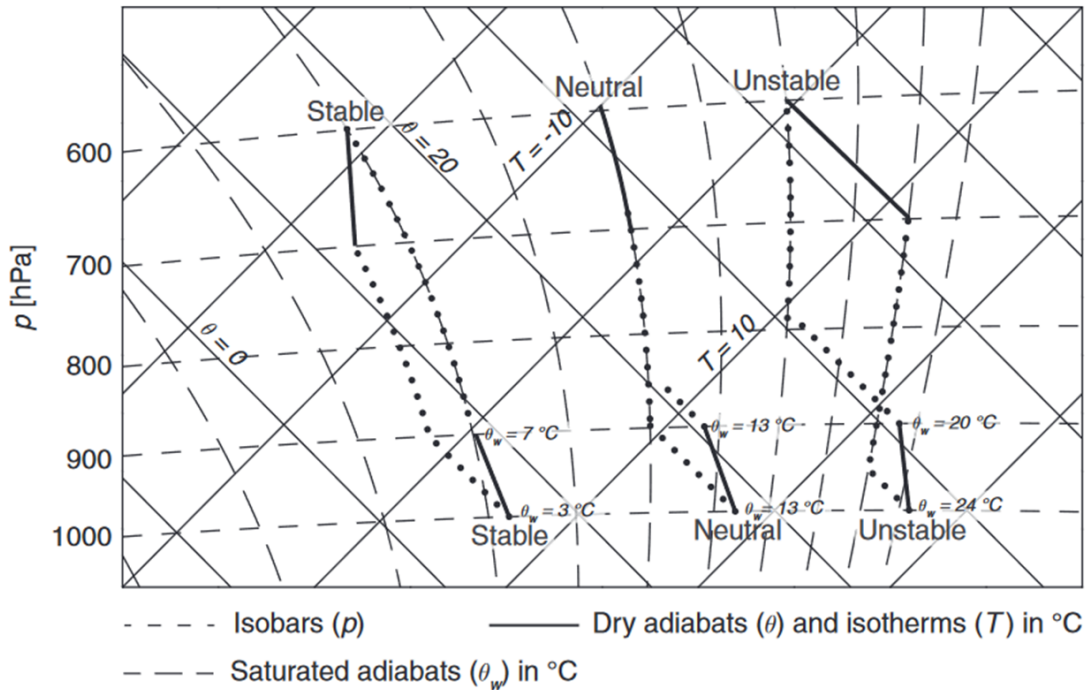


Figure 3.4: Skew T -  $\ln p$  diagram to illustrate potential instability when a layer of moist air is lifted from between 1000 and 900 hPa to between 700 and 600 hPa. The bold solid lines represent the lapse rate in the layer before and after lifting. The dotted lines show the ascent of the top and the bottom of the layer. Fig. 3.4 of Lohmann, Lüönd, and Mahrt (2016).

### 3.4 CIN and CAPE

The concept of buoyancy allows us to develop a perspective on atmospheric convection. In short, CIN is the negative buoyancy vertically integrated over the near surface atmosphere that present a “barrier” to convective motions. CAPE is the positive buoyancy vertically integrated further above, roughly speaking in the free troposphere up to the tropopause, and represents the maximum possible energy that can be released (e.g., converted to kinetic energy) by the parcel after the CIN barrier has been overcome.

$$CIN = - \int_0^{z_{LFC}} b(z) dz = - \int_0^{z_{LFC}} \left[ \frac{T_v - T_{v,env}}{T_{v,env}} \right] g dz$$

Note that because CIN is defined with a minus sign and  $b < 0$ , CIN has positive values.

We can rewrite this for pressure coordinates by means of the hydrostatic equation and ideal gas law. Rewriting for  $p$  is helpful for the skew T - ln p diagram. Recall the hydrostatic balance,  $dp = -\rho g dz$  and the, ideal gas law for moist air,  $p = \rho R_d T_{v,env}$ .

$$\begin{aligned} dp &= -g \frac{p}{R_d T_{v,env}} dz \\ -\rho g dz &= -g \frac{p}{R_d T_{v,env}} dz \\ g \frac{dz}{T_{v,env}} &= -\frac{R_d}{p} dp = -R_d dlnp \end{aligned}$$

Hence, CIN is given by

$$CIN = R_d \int_{p_{sf}}^{p_{LFC}} \underbrace{(T_v - T_{v,env})}_{\approx T - T_{env}} dlnp \approx R_d \int_{p_{sf}}^{p_{LFC}} (T - T_{env}) dlnp.$$

Similary, for CAPE one can derive

$$\begin{aligned} CAPE &= \int_{z_{LFC}}^{z_{EL}} b(z) dz \\ &= \int_{z_{LFC}}^{z_{EL}} \left[ \frac{T_v - T_{v,env}}{T_{v,env}} \right] g dz \\ &= R_d \int_{p_{LFC}}^{p_{EL}} \underbrace{(T_{v,env} - T_v)}_{\approx T_{env} - T} dlnp \\ &\approx R_d \int_{p_{LFC}}^{p_{EL}} (T_{env} - T) dlnp \end{aligned}$$

CIN and CAPE are hence closely related, but because CIN is defined with a minus sign, the order of terms in the equations are swapped between the two quantities.

The concepts of CIN and CAPE are illustrated in Figure 3.5 for an environmental sounding (for example obtained from a weather balloon) and an assumed adiabatic displacement of an air parcel from the surface upward. Besides CIN and CAPE, the figure introduces a few additional quantities.

- LCL: lifting condensation level (at this level clouds typically start to form)
- LFC: level of free convection (at this level the parcel temperature becomes larger than the environmental temperature)
- EL: equilibrium level (at this level the parcel temperature stops to be larger than the environmental temperature)

CIN and CAPE are proportional to the gray areas enclosed by the temperature profiles of the parcel and the environment.

Examples for soundings are available, for example, at <https://www.weather.gov/upperair/sounding> and [https://www.aos.wisc.edu/weather/wx\\_obs/Soundings.html](https://www.aos.wisc.edu/weather/wx_obs/Soundings.html).

### 3.5 Km-scale simulations to compute convection explicitly

[https://www.youtube.com/watch?v=llOh7N\\_VY7k](https://www.youtube.com/watch?v=llOh7N_VY7k)

<https://www.youtube.com/watch?v=EzqjAFJYmgY>

### 3.6 What is the fundamental modeling problem in representing convection and turbulence?

To understand why representing convection and turbulence in models is a hard problem, we first need to briefly discuss the equations that describe the dynamics and thermodynamics of the moist atmosphere. This set of equations is called “primitive equations”.

$$\begin{aligned} \frac{D\vec{v}}{Dt} + 2\vec{\Omega} \times \vec{v} &= -\frac{1}{\rho} \nabla p - \vec{g} + \vec{F}_v \\ \frac{\partial \rho}{\partial t} + \nabla \cdot (\rho \vec{v}) &= 0 \\ c_v \frac{DT}{Dt} + p \frac{D\alpha}{Dt} &= Q \\ \frac{\partial \rho q_i}{\partial t} + \nabla \cdot (\rho q_i \vec{v}) &= X_i \\ p &= \rho R_d T_v \end{aligned}$$

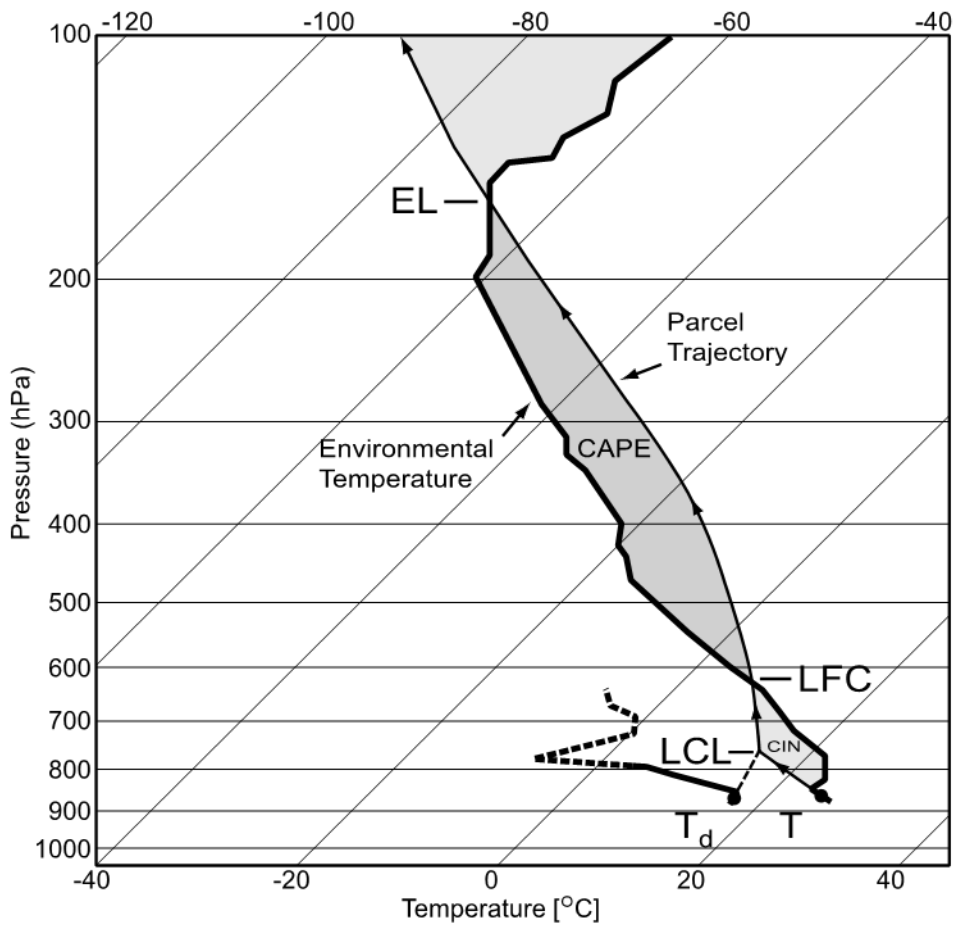


Figure 3.5: Fig. 8.10 of G. W. Petty (2008).

The first equation is a vector equation for the 3-dimensional wind  $\vec{v} = (u, v, w)$ , and is nothing else than Newton's first law  $\vec{F} = m\vec{a}$  for a fluid under the influence of rotation.  $\frac{D}{Dt}$  is the material or total derivative that includes the local time derivative and advection,  $\vec{\Omega}$  is the angular velocity of the rotating Earth,  $\rho$  is the air density,  $p$  is pressure,  $\vec{g}$  is the gravitational acceleration, and  $\vec{F}_v$  describes the effect of friction on the wind field.

The second equation is the continuity equation, which describes that the total atmospheric mass cannot be lost or gained, at least on the timescales that we consider. Strictly speaking, the equation is only valid for the dry mass of the atmosphere, as moisture can be lost or gained through precipitation and evaporation at the surface.

The third equation is the first law of thermodynamics, and describes changes in temperature through advection by the wind field (taken into account by the material derivative  $D/Dt$ ), the pressure-volume work, and the sum of diabatic processes  $Q$ , which, for example, include radiation and latent heating by condensation of water vapor.

The fourth equation is actually several equations, one each for each species of atmospheric moisture that is considered. It is often sufficient to only consider water vapor  $q$ , but one could also include equations for other species such as cloud liquid water, cloud ice and rain.  $X_i$  describes the sources and sinks of for a given form of atmospheric moisture, such as the loss of water vapor through the condensation of water vapor onto cloud droplets.

Finally, the last equation is the equation of state, written with the virtual temperature  $T_v$  to take into account the effect of water vapor.

The primitive equations are a set of non-linear, partial differential equations, and incorporate the many scales of atmospheric motions, from the planetary scales of the Rossby waves (i.e., the meandering jet stream in the extratropics) and the Hadley circulation in the tropics, to the small scales of individual thunderstorms, clouds and turbulence. The vast range of scales of atmospheric motions that are described by primitive equations is illustrated in Figure 3.6, with the primitive equations describing phenomena with length scales of roughly 1km and larger.

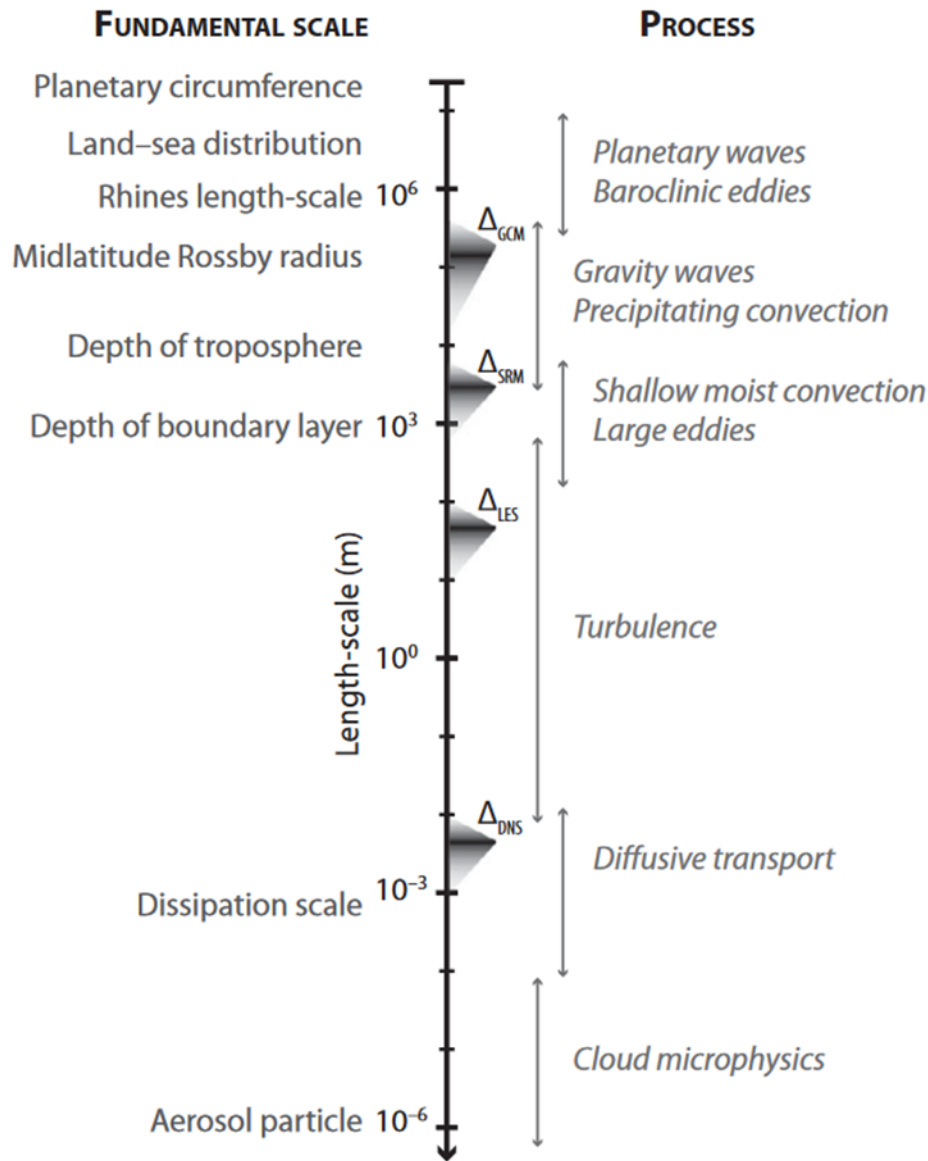


Figure 3.6: Fig. 2.13 of Siebesma et al. (2020).

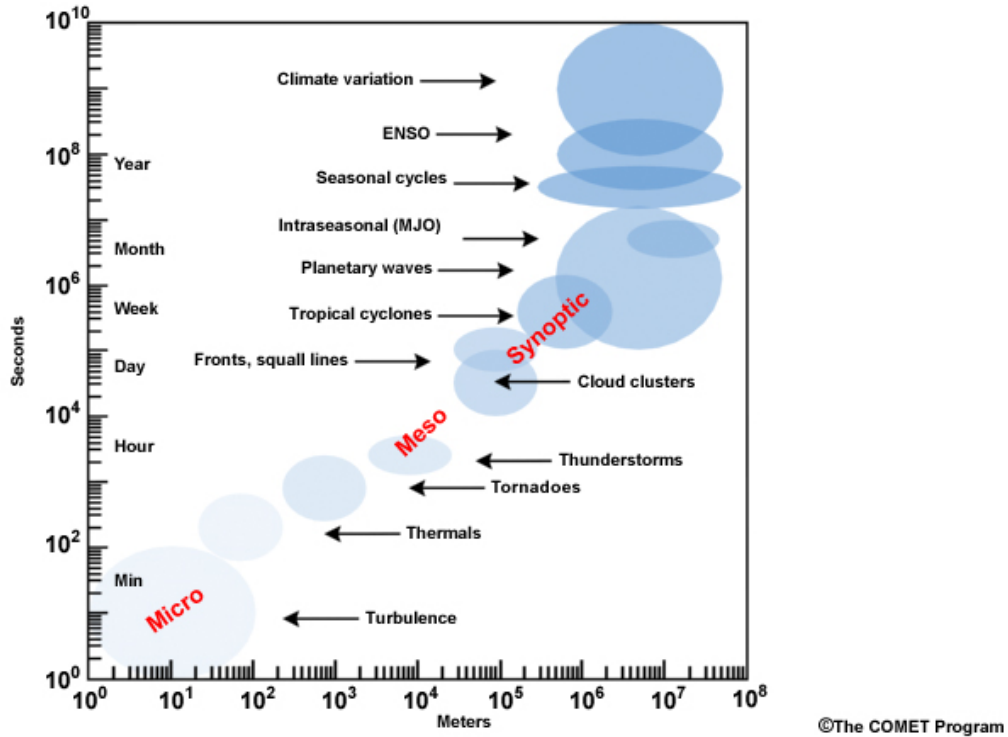


Figure 3.7: Spatiotemporal scales of atmospheric motions. Figure from the COMET Program, <https://www.meted.ucar.edu/index.php>.

It is impossible in a climate and weather model to include all relevant scales from Figure 3.6. This means that the equations need to be “truncated” at a given scale, where the scale is given by the discretization used for a model’s numerical scheme. This means that process and phenomena that operate on scales below the chose truncation cannot be simulated “explicitly” or “resolved”. Still, their impact on the larger scales that are simulated explicitly and are hence resolved needs to be taken into account. An concrete example here are the convective motions on horizontal scales of 1-10km. These motions are fundamental to the vertical distribution of temperature and moisture and thereby influence motions on much larger scales, such as extratropical cyclones and the Hadley circulation, whose dynamics depend, among other factors, on the stability or “stratification” of the atmosphere.

One might wonder if it was possible to compute the effect of the unresolved scales on the resolved scales in an exact manner. In the following, we discuss why this is fundamentally impossible. This impossibility is often referred to as the turbulence closure problem.

To understand the turbulence closure problem, it is illustrative to consider a simplified problem: a 2-dimensional incompressible fluid without rotation and without friction. I.e.,

$$\begin{aligned}
\vec{v} &= (u, v, 0) = (u_1, u_2), \\
\vec{g} &= (0, 0), \\
\rho &= \rho_c = \text{const.}, \\
\vec{\Omega} &= (0, 0), \\
\vec{F}_v &= (0, 0).
\end{aligned} \tag{3.1}$$

To allow for a more compact notation, we use the Einstein convention of summing over repeated indices. For example, for the advection of the zonal wind component:

$$u_j \frac{\partial u_1}{\partial x_j} = u_1 \frac{\partial u_1}{\partial x_1} + u_2 \frac{\partial u_1}{\partial x_2} = u \frac{\partial u}{\partial x} + v \frac{\partial v}{\partial y}.$$

With these simplifications, we can write the momentum equation as

$$\frac{Du_i}{Dt} = \frac{\partial u_i}{\partial t} + u_j \frac{\partial u_i}{\partial x_j} = -\frac{1}{\rho_c} \frac{\partial p}{\partial x_i} \tag{3.2}$$

We now use “Reynolds-averaging” and expand each variable into a mean, denoted by  $\bar{\cdot}$ , and a perturbation, denoted by  $'$ . The mean represents the variable’s value on the truncated scale (e.g., the size of the grid box of a model), the perturbation represents the variable’s value on smaller scales. Using the terminology from above, the mean is explicitly simulated and resolved, whereas the perturbation is not. The perturbation is often referred to a “small-scale” or “subgrid-scale”.

To be explicit, the expansion is given by

$$\begin{aligned}
u_i &= \bar{u}_i + u'_i, \\
p &= \bar{p} + p'.
\end{aligned}$$

Then, the momentum equation can be expanded as well:

$$\begin{aligned}
\frac{Du_i}{Dt} &= \frac{D(\bar{u}_i + u'_i)}{Dt} = \dots \\
&= \frac{\partial \bar{u}_i}{\partial t} + \frac{\partial u'_i}{\partial t} + \bar{u}_j \frac{\partial \bar{u}_i}{\partial x_j} + \bar{u}_j \frac{\partial u'_i}{\partial x_j} + u'_j \frac{\partial \bar{u}_i}{\partial x_j} + u'_j \frac{\partial u'_i}{\partial x_j} \\
&= -\frac{1}{\rho_c} \frac{\partial \bar{p}}{\partial x_i} - \frac{1}{\rho_c} \frac{\partial p'}{\partial x_i}.
\end{aligned} \tag{3.3}$$

Because we are only interested in the evolution of the mean, we compute the “mean” of the above equation. All terms linear in a perturbed variable drop out, while correlations of perturbed variables remain.

$$\frac{D\bar{u}_i}{Dt} = \frac{\partial \bar{u}_i}{\partial t} + \bar{u}_j \frac{\partial \bar{u}_i}{\partial x_j} + \overline{+u'_j \frac{\partial u'_i}{\partial x_j}} = -\frac{1}{\rho_c} \frac{\partial \bar{p}}{\partial x_i}$$

When rearranging slightly to

$$\frac{\partial \bar{u}_i}{\partial t} + \bar{u}_j \frac{\partial \bar{u}_i}{\partial x_j} + = -\frac{1}{\rho_c} \frac{\partial \bar{p}}{\partial x_i} - \overline{u'_j \frac{\partial u'_i}{\partial x_j}},$$

we find a “new” term that was absent in the original equation before truncation and Reynold’s averaging. This new term is the mean of a correlation function: the mean of velocity perturbations advected by velocity perturbations. Because the term is on the r.h.s. of the equation, we need to compute it to compute the evolution of the mean velocity field.

One can further use the continuity equation for  $\rho_c = const.$  to write the new term as a stress term.

$$\begin{aligned}\frac{\partial u_j}{\partial x_j} &= 0 \\ \frac{\partial u'_j}{\partial x_j} &= 0 \\ \overline{u'_j \frac{\partial u'_i}{\partial x_j}} &= \overline{\frac{\partial u'_j u'_i}{\partial x_j}}\end{aligned}$$

With this,

$$\frac{\partial \bar{u}_i}{\partial t} + \bar{u}_j \frac{\partial \bar{u}_i}{\partial x_j} + = -\frac{1}{\rho_c} \frac{\partial \bar{p}}{\partial x_i} - \overline{\frac{\partial u'_j u'_i}{\partial x_j}}, \quad (3.4)$$

where the last term is referred to as “Reynold stress” and is given by the covariance of the perturbation terms or turbulent terms.

To predict the evolution of the mean field, we need to compute the Reynold stress. We now derive an equation of the time evolution of the Reynold stress by subtracting Equation 3.4 from Equation 3.3. This yields an equation for the evolution of the perturbation terms:

$$\frac{\partial u'_i}{\partial t} + \bar{u}_j \frac{\partial u'_i}{\partial x_j} + u'_j \frac{\partial \bar{u}_i}{\partial x_j} + u'_j \frac{\partial u'_i}{\partial x_j} = -\frac{1}{\rho_c} \frac{\partial p'}{\partial x_i} + \overline{\frac{\partial u'_j u'_i}{\partial x_j}}.$$

What now follows are a number of steps that include multiplying the equation by  $u'_k$ , using  $\frac{\partial u'_i u'_k}{\partial t} = u'_i \frac{\partial u'_k}{\partial t} + u'_k \frac{\partial u'_i}{\partial t}$ , changing indices from  $i$  to  $k$  etc. For details, see Eqs. 5.13-5.15 of Stensrud (2007).

The result is equations for the Reynold stresses:

$$\begin{aligned} \frac{\partial \overline{u'_i u'_k}}{\partial t} + \overline{u}_j \frac{\partial \overline{u'_i u'_k}}{\partial x_j} = \\ - \overline{u'_i u'_j} \frac{\partial \overline{u}_k}{\partial x_j} - \overline{u'_k u'_j} \frac{\partial \overline{u}_i}{\partial x_j} - \frac{\partial \overline{u'_i u'_j u'_k}}{\partial x_j} \\ - \frac{1}{\rho_c} \left[ \frac{\partial \overline{p' u'_k}}{\partial x_i} + \frac{\partial \overline{p' u'_i}}{\partial x_k} - \overline{p'} \left( \frac{\partial \overline{u'_i}}{\partial x_k} + \frac{\partial \overline{u'_k}}{\partial x_i} \right) \right]. \end{aligned}$$

Hence, while we have found equations to compute the evolution of the Reynold stresses, these equations include triple correlation terms of the form

$$\frac{\partial \overline{u'_i u'_j u'_k}}{\partial x_j}.$$

These again are not known, and all we have achieved is to shift the problem from one set of unknown quantities to another set of unknown quantities! This cascade of unknowns is the turbulence closure problem. A consequence of the turbulence closure problem is that “parametrizations” are needed to relate the unknown Reynold stress terms to the known mean fields.

### 3.7 Parametrizations of subgrid-scale processes

The “turbulence closure problem” showed that it is impossible to derive closed equations for the perturbation quantities with scales smaller than the spatial and time resolution of a model or a measurement apparatus. However, as shown by Equation 3.4, information about these subgrid-scale quantities is essential for calculating the evolution of mean quantities.

This information is provided by parameterizations, which represent the effects of subgrid-scale quantities on the resolved mean quantities. Importantly, parameterizations do not represent the subgrid-scale quantities themselves—these are unnecessary for evolving the mean quantities over time. Subgrid-scale processes are crucial for many aspects of weather and climate, particularly those related to clouds and convection, which impact global water and energy cycles and, consequently, atmospheric motions on all scales.

Parameterizations aim to represent the effects of subgrid-scale processes on the resolved flow, often using semi-empirical parametric functions or, more recently, machine-learned functions. Since only grid-scale information is available, parameterizations must express the impact of subgrid-scale fields as a function of the grid-scale fields - it is not difficult to imagine that this is challenging task.

Parametrizations form the so-called “physics” component of any weather and climate model. They need to be distinguished from the “so-called” dynamical cores of models that describe the scales of motions that are directly simulated (i.e., “resolved”) by the truncated set of equations solved by the model. Which motions are resolved depends on the grid spacing: with finer grid spacing, more motions can be simulated directly, reducing the need for parameterizations. As a general rule, the finer the model’s resolution, the fewer parameterizations are required. Parameterizations thus depend on a model’s grid spacing, a concept sometimes referred to as “scale-aware” parameterizations.

In equation Equation 3.1, the two components of the model can be distinguished if we interpret the variables as mean quantities, following Reynold’s averaging, or as resolved quantities according to the model’s spatial and temporal resolution. In this context,  $\vec{F}_v$ ,  $Q$ , and  $X_i$  make up the physics component and, through parameterizations, represent processes such as:

- Cloud formation and precipitation ( $Q$ ,  $X_i$ )
- Radiative transfer ( $Q$ )
- Surface interactions ( $\vec{F}_v$ ,  $Q$ ,  $X_i$ )
- Turbulence and convection ( $\vec{F}_v$ ,  $Q$ )

By contrast, the dynamical core includes all other terms in Equation 3.1: advection, rotation, the pressure-gradient force, pressure-volume work, and the equation of state. In practice, the physics component and the dynamical core are implemented as separate parts within the source code of models, as illustrated in Figure 3.8.

To time step the state of the atmosphere, ocean, land and other components forward, the model combines the time tendency calculated from its dynamical with that calculated from its physics. That is,

$$\frac{\partial x}{\partial t} = \left. \frac{\partial x}{\partial t} \right|_{\text{dynamical core}} + \left. \frac{\partial x}{\partial t} \right|_{\text{physics}},$$

where  $x$  stands for temperature, the 3-dimensional wind field, specific humidity etc. The combined local time derivative is then used with a time integration scheme such as Runge-Kutta to compute the state at the next time step.

Figure 3.9 presents the temperature tendencies from various parameterizations in the EC-Earth climate model. Although specific contributions and distributions of these parameterized tendencies differ among models, this example illustrates the typical contributions and spatial patterns of four common parameterization types.

Panel a shows the effect of parameterized cumulus convection. Cumulus convection schemes simulate how cumulus clouds transport heat, moisture, and momentum from the boundary layer into higher levels of the atmosphere. As condensation occurs, it releases latent heat, causing the air within cumulus clouds to become buoyant; this drives strong vertical movement up to the tropopause. This type of convection is the primary mechanism for vertical transport

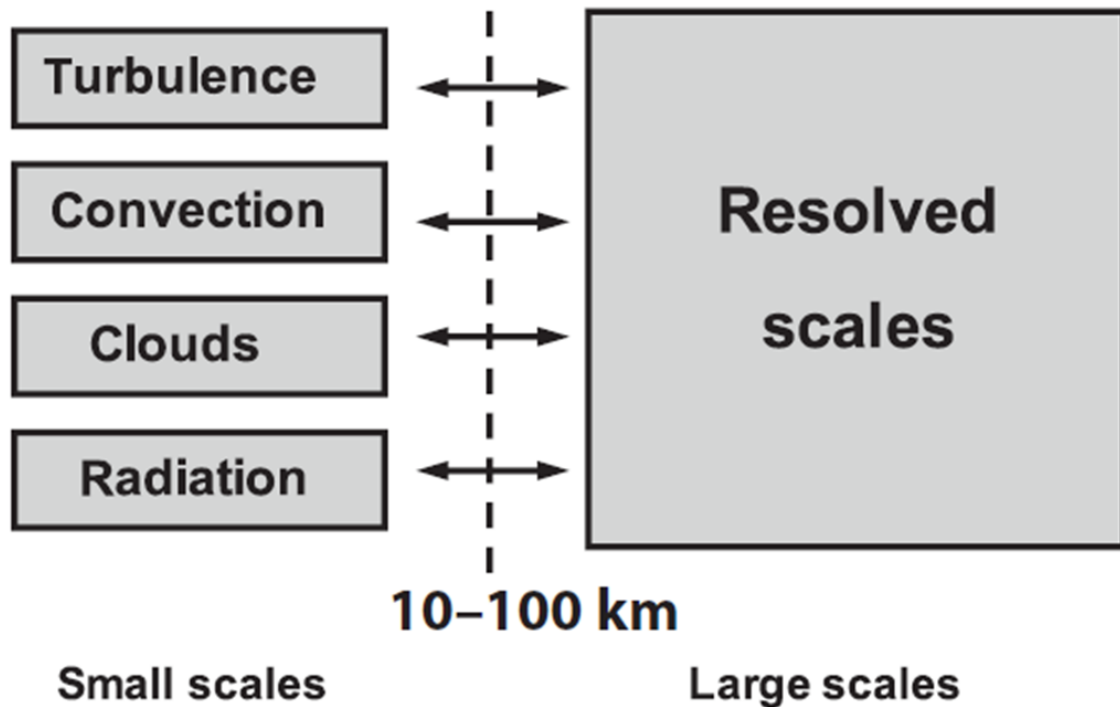


**FIGURE 6.2:** Depiction of the interaction between resolved and parameterised unresolved cloud-related processes (convection, turbulence, clouds and radiation) in traditional climate models.

Figure 3.8: Fig. 6.2 of Siebesma et al. (2020). The processes on the l.h.s. are modeled by parametrizations that form the physics component of models. The r.h.s. is the dynamical core that computes the resolved quantities. One typically refers to small-scale quantities as subgrid-scale quantities and to large-scale quantities as resolved quantities.

out of the planetary boundary layer and serves as a significant source of precipitation. In the tropics, this process produces substantial heating, reaching up to 7 K per day, whereas in the subtropics, the downward motion of air in the descending part of the Hadley circulation limits its reach and intensity. Near the surface, cumulus convection leads to cooling as heat is vented into the free atmosphere.

Panel b illustrates radiative heating and cooling as calculated by the radiation scheme. Throughout the troposphere, radiation has a relatively uniform cooling effect of 1–2 K per day. Above the tropical tropopause, around 100 hPa and above, radiation heats the atmosphere due to the absorption of solar radiation by stratospheric ozone. We will discuss radiation in more detail in later chapters.

Panel c demonstrates the effects of the cloud scheme. Cloud schemes estimate essential cloud properties—such as cloud fraction, water/ice content, and droplet density for both convective and non-convective clouds. They also determine precipitation amounts for non-convective (large-scale) clouds. While their overall heating effect is generally small and often negative, since most condensational heating is accounted for by the convection scheme, cloud schemes are crucial for representing cloud characteristics in the model. Note that the negative heating occurs because of the evaporation of cloud droplets and rain, and the melting of cloud ice crystals and snow.

Panel d shows the effect of boundary-layer turbulence, which warms the lowest kilometers of the atmosphere, particularly in low-latitude regions. This warming results from the turbulent mixing of surface sensible heat flux into the planetary boundary layer. Similarly, by vertically transporting moisture from surface evaporation, boundary-layer turbulence has a net annual effect of moistening the boundary layer, most notably over low-latitude oceans. Interestingly, boundary-layer turbulence has a cooling effect over the Antarctic ice sheet. This happens because in contrast to other regions, the ice sheet surface is colder than the overlying atmosphere, meaning that the atmosphere is cooled by downward transport of sensible heat.

## 3.8 Representing convection in atmospheric models

### 3.8.1 Hard convective adjustment

Hard convective adjustment, developed by Syukuro Manabe and colleagues in the 1960s, is a simple and computationally efficient way to represent moist convection in early climate models. The method involves adjusting the atmospheric temperature profile whenever it becomes statistically unstable. This approach assumes that convective processes will act quickly to remove any instability by modifying the temperature and moisture profiles, effectively maintaining a state close to neutral buoyancy.

As discussed earlier, convection, i.e., the need for vertical exchanges of energy, is triggered when air becomes warmer and lighter (less dense) than the air above it. This situation creates

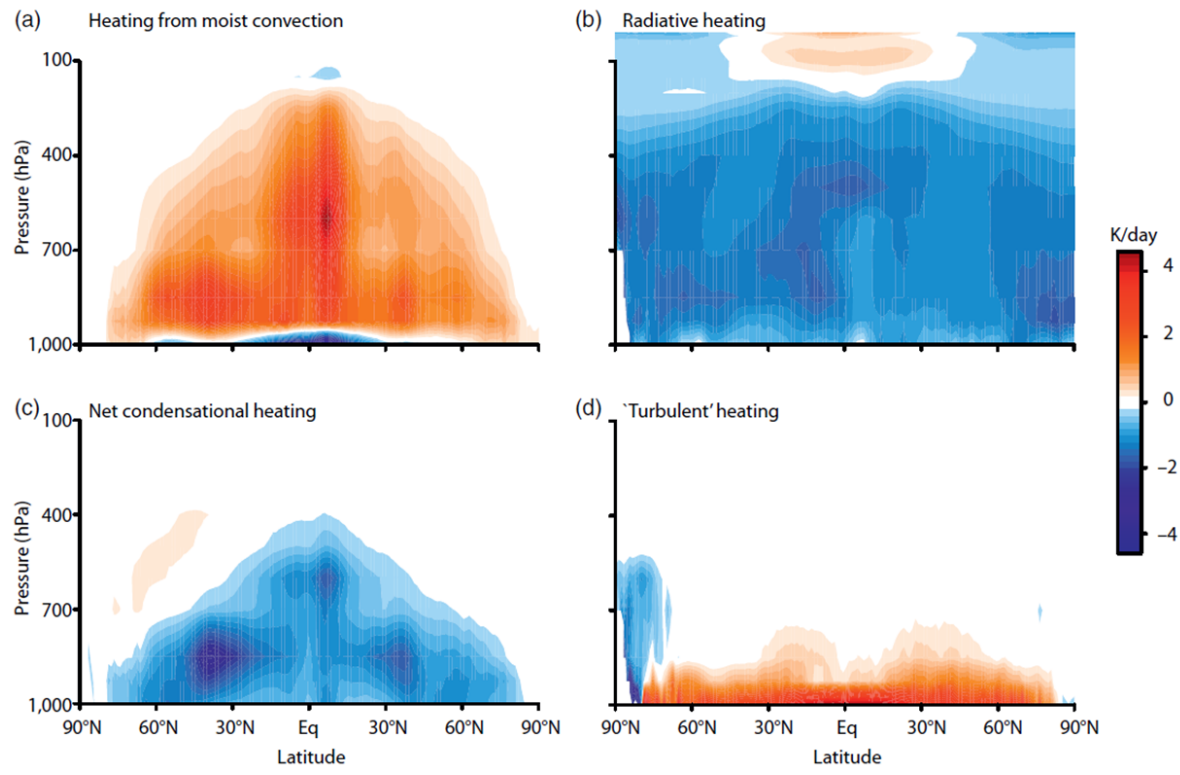


Figure 3.9: Fig. 6.3 of Siebesma et al. (2020).

static instability, which causes the warm air to rise until the temperature profile reaches a stable state. Hard convective adjustment is based on the principle that convection removes static instability immediately and brings the atmosphere back to a stable, moist adiabatic profile. While this is an idealization and convection is not instantaneous, this assumption is justified to first order because convection is much faster than other processes, most notably radiation. A typical time scale for convection is a few hours but many hours to days for radiation.

The basic idea is to adjust the temperature profile so that it adheres to the moist adiabatic lapse rate, defined as:

$$\Gamma_m = -\frac{dT}{dz},$$

where  $\Gamma_m$  is the moist adiabatic lapse rate and  $\frac{dT}{dz}$  is the vertical gradient of temperature  $T$  with respect to height  $z$ .

The adjustment begins by identifying regions of the atmosphere where the calculate lapse rate exceeds the moist lapse rate,

$$\Gamma > \Gamma_m.$$

When this condition is met, hard convective adjustment adjusts the temperature profile so that the lapse rate matches the moist adiabatic rate. The principle works as follows:

1. Identify model levels with  $\Gamma > \Gamma_m$ .
2. Adjust the temperature of the unstable levels from  $T$  to  $T^* = T + \delta T$  so that  $\frac{\partial T^*}{\partial z} = -\Gamma_m$ .
3. Conserve energy: convection redistributes energy vertically and conserves column-integrated energy. This is ensured by integrating  $\delta T$  vertically over the adjusted layers and demanding that

$$\frac{c_p}{g} \int_0^{p_{sfc}} \delta T dp = \chi = 0,$$

where  $c_p$  is the specific heat capacity of air,  $g$  is gravitational acceleration,  $p_{sfc}$  is the surface pressure, and we have for simplicity assumed that there was no energy exchange with the surface. If the integral on the l.h.s. does not fullfil  $\chi = 0$ , then  $\delta T$  is changed to  $\delta T - \chi$ .

At the end of step 3, the initial instability is removed, but new instabilities might have been created at the boundaries of the initially unstable layer. It might thus be necessary to repeat steps 1-3 in an iterative manner (see Akmaev (1991) and the appendix of Kluft et al. (2019)). It should also be noted that some models implement hard convective adjustment as a time

tendency in the models, e.g. Manabe and Strickler (1964), whereas the principle described above adjusts a given temperature profile instantaneously.

The method is straightforward and computationally inexpensive, making it suitable for early climate models with limited computing power. However, it has limitations. First, it is a simplified representation of convection that does not explicitly simulate the vertical transport of moisture or the dynamic processes within convective clouds. And second, it assumes that convection is instantaneous. For considerations on climate time scales, this assumption might be warranted, but for shorter time scales of weather, this assumption is not warranted: for example, rainfall over tropical land does not peak at local noon when solar insolation and the destabilization of the atmosphere is strongest; rather it peaks several hours later in the late afternoon.

Despite these limitations, hard convective adjustment was instrumental in the development of early climate models and laid the groundwork for more complex convection schemes used in modern models and for building understanding. For example, it provided a basis for the development of simple yet powerful theoretical frameworks such as “quasi-equilibrium” adjustments, and it continues to be used in many simplified climate models, such as [Konrad](#), [climlab](#) and [CLiMT](#).

JULY 1964

SYUKURO MANABE AND ROBERT F. STRICKLER

361

## Thermal Equilibrium of the Atmosphere with a Convective Adjustment

SYUKURO MANABE AND ROBERT F. STRICKLER

*General Circulation Research Laboratory, U. S. Weather Bureau, Washington, D. C.*  
(Manuscript received 19 December 1963, in revised form 13 April 1964)

### ABSTRACT

The states of thermal equilibrium (incorporating an adjustment of super-adiabatic stratification) as well as that of pure radiative equilibrium of the atmosphere are computed as the asymptotic steady state approached in an initial value problem. Recent measurements of absorptivities obtained for a wide range of pressure are used, and the scheme of computation is sufficiently general to include the effect of several layers of clouds.

The atmosphere in thermal equilibrium has an isothermal lower stratosphere and an inversion in the upper stratosphere which are features observed in middle latitudes. The role of various gaseous absorbers (i.e., water vapor, carbon dioxide, and ozone), as well as the role of the clouds, is investigated by computing thermal equilibrium with and without one or two of these elements. The existence of ozone has very little effect on the equilibrium temperature of the earth's surface but a very important effect on the temperature

Figure 3.10: Section 2 of Manabe and Strickler (1964) describes the original implementation of hard convective adjustment.

### 3.8.2 Mass-flux schemes

Mass flux schemes partition the grid box into a convecting and a non-convecting portion (Figure 3.11). The convective portion represents the rising air within convective clouds, while the non-convective portion represents the surrounding, typically more stable, environment.

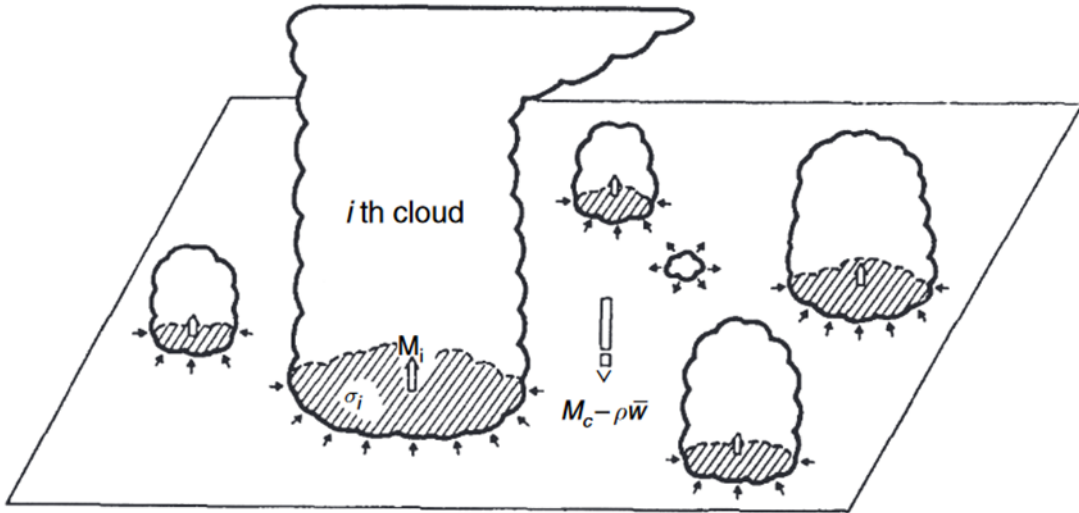


Figure 3.11: Fig. 6.6 of Stensrud (2007).

In the convecting portion, specific rules are applied to neutralize the profile. As the convective air rises, it interacts with the surrounding non-convective air. This process involves entrainment, where surrounding air is drawn into the convective plume, and detrainment, where air within the plume is deposited back into the surrounding environment. Entrainment and detrainment rates play a crucial role in determining how much air is mixed between the convective and non-convective parts and, therefore, in shaping the overall effects of convection. The schemes then calculate a subgrid-scale convective mass flux, which determines the vertical mixing of temperature and moisture.

Mass flux schemes are used in models with grid spacings that are too coarse to resolve individual convective clouds (typically around 100km), such as in climate models used for the Coupled Model Intercomparison Project (CMIP). However, the parameterization of entrainment and detrainment rates, as well as the trigger conditions that initiate convection, can vary widely between models and are difficult to constrain by observations and theories. These variations can introduce large uncertainties in model results, as different formulations can produce different representations of convective effects on climate. Some of these uncertainties are illustrated in Figure 3.12, Figure 3.13, Figure 3.14 and Figure 3.15.

Figure 3.12 shows simulations of the African rainfall in the present-day climate and its response to a uniform 2K warming of the ocean surface in two version of the AM2.1 global

climate model. The two versions only differ in their treatment of convection: one version uses the RAS parametrization, the other version uses the UW parameterization. The change in parameterization leads to profound differences in the simulation of precipitation in the present-day climate, with the RAS scheme producing substantially more precipitation. The two versions also simulate contradicting changes in precipitation with warming: while Sahel precipitation decreases with the RAS scheme, it increases with the UW scheme.

The left panel of Figure 3.13 shows aquaplanet simulations with several 100km atmosphere models and prescribed sea-surface temperatures, with all models using mass flux schemes. The right panel shows simulations with a single model but with different versions of its mass flux scheme. In both cases, differences in the treatment of convection lead to stark differences in the simulated rainfall, with some models putting the rainfall maximum at the equator, while others simulate the maximum rainfall 10 deg latitude away from the equator.

Figure 3.14 compares precipitation simulated in a 100km climate model with a mass flux scheme (AMIP) and with the convection parametrization disabled (ConvOff). While the latter is a drastic choice, the time-mean precipitation is not strongly sensitive to the treatment of convection in the used model. However, without a convection scheme, the model produces excessive extreme rainfall.

Figure 3.15 shows the mean diurnal cycle of precipitation over local time for Africa (August 2016) in observations, the 100km climate model ECHAM with a mass-flux convection scheme, and the km-scale model ICON-SRM with 2.5km grid spacing and explicit convection. While the km-scale model captures the precipitation evolution well, the 100km model produces too much precip to early in the day. This problem is typical for mass flux schemes.

### 3.8.3 Superparametrization

Superparametrization embeds a 2D or 3D cloud-resolving model with a mesh of  $dx \approx 1\text{km}$  into each grid box of the coarse “parent” model with  $dx \approx 100\text{km}$ . The fine resolution of the embedded cloud-resolving model allows one to resolve (some of the) convection and cloud processes that the parent model cannot directly simulate due to its larger grid boxes.

The embedded cloud-resolving model receives data about temperature, water vapor etc. from the parent model. This allows it to simulate the formation and behavior of clouds and convection explicitly without using a convective parametrization. The cloud-resolving model runs for the duration of the parent model’s time step, and then sends the results — such as changes in temperature, moisture, and momentum — back to the parent model. This feedback helps the parent model make more accurate predictions about weather and climate.

By incorporating a cloud-resolving model directly into the grid boxes of a larger model, superparameterization enhances the representation of convection and cloud processes, leading to improved accuracy in simulating precipitation, temperature, and other atmospheric phenomena.

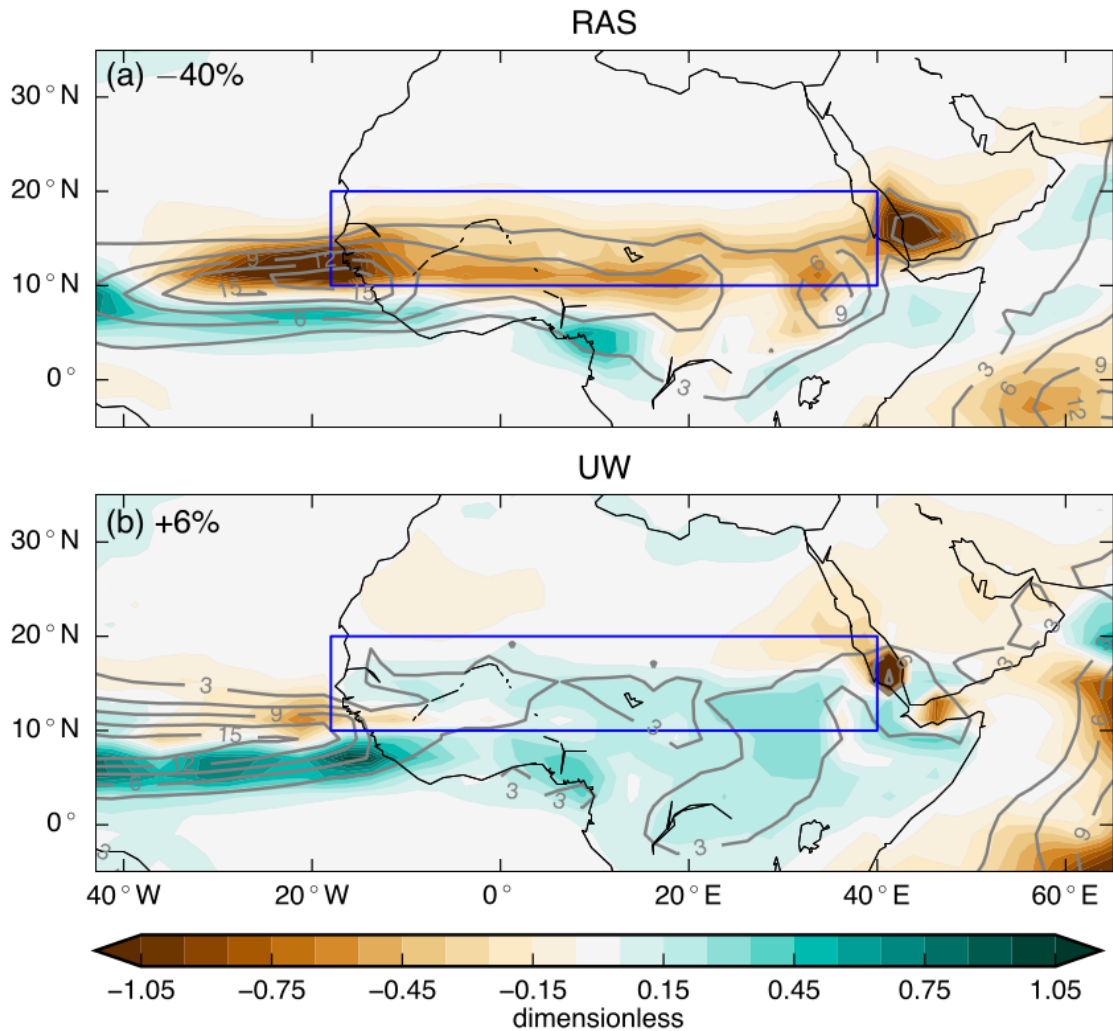


Figure 3.12: Change in precipitation between the uniform 2-K SST warming and present-day control simulations for two versions of the AM2.1 global climate model. The precipitation change is normalized by the Sahel-mean precipitation in the control simulation and therefore unitless. The precipitation change is shown by the shaded contours; precipitation in the control simulation is shown by the gray contours. The blue box is the Sahel region. Fig. 1 of Hill et al. (2017).

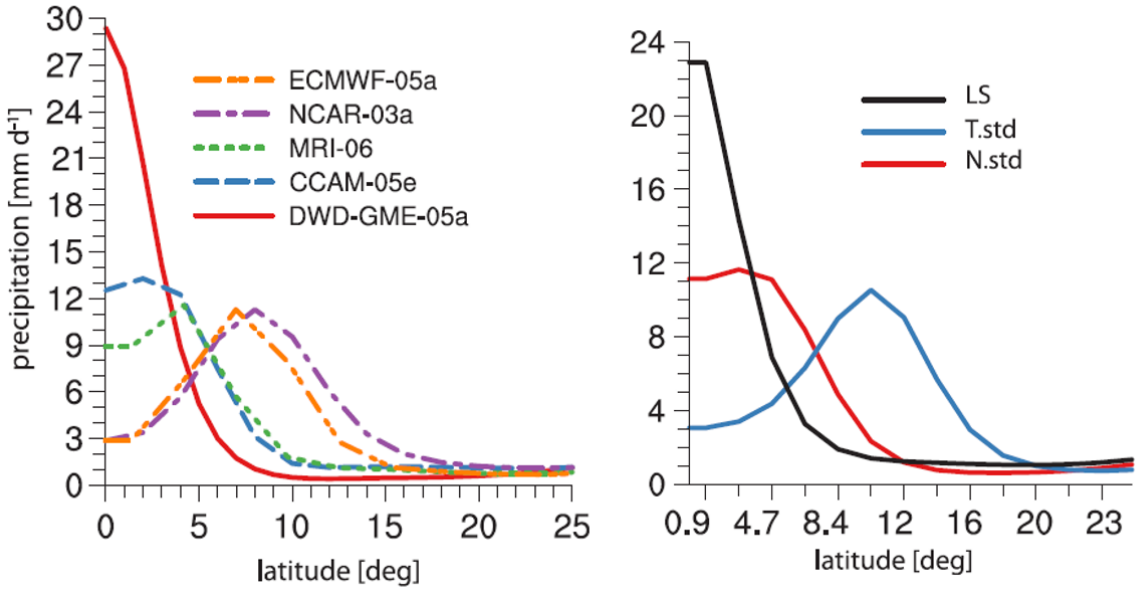


Figure 3.13: Figs. 4 and 3a Möbis and Stevens (2012).

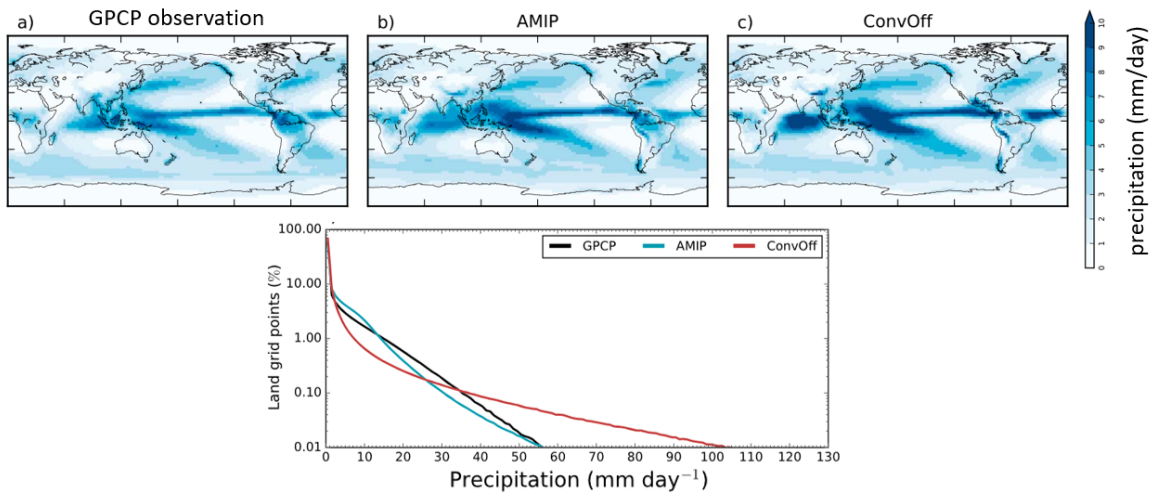


Figure 3.14: Figs. 1 and 2b of Maher et al. (2019). The left panel in the top row shows observations.

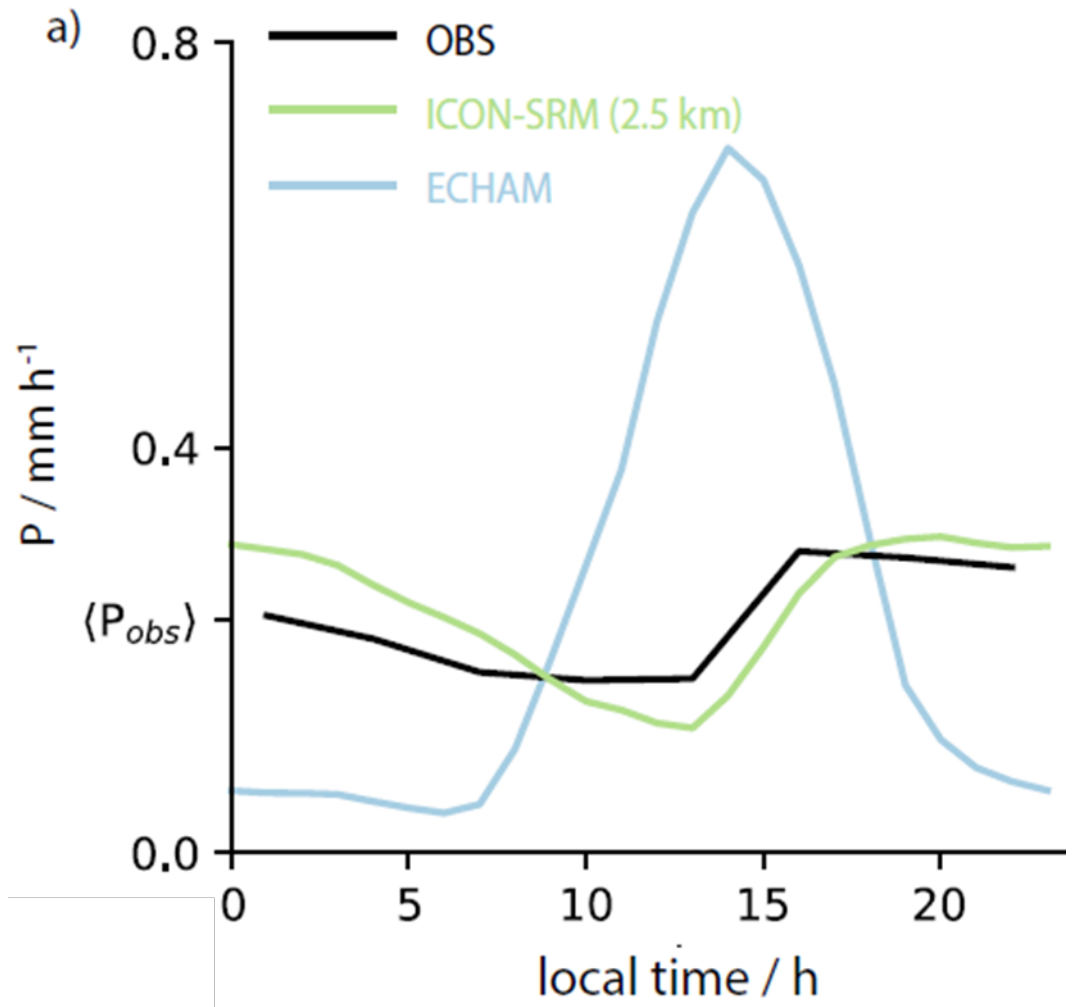


Figure 3.15: Fig. 12 of Bjorn Stevens et al. (2020).

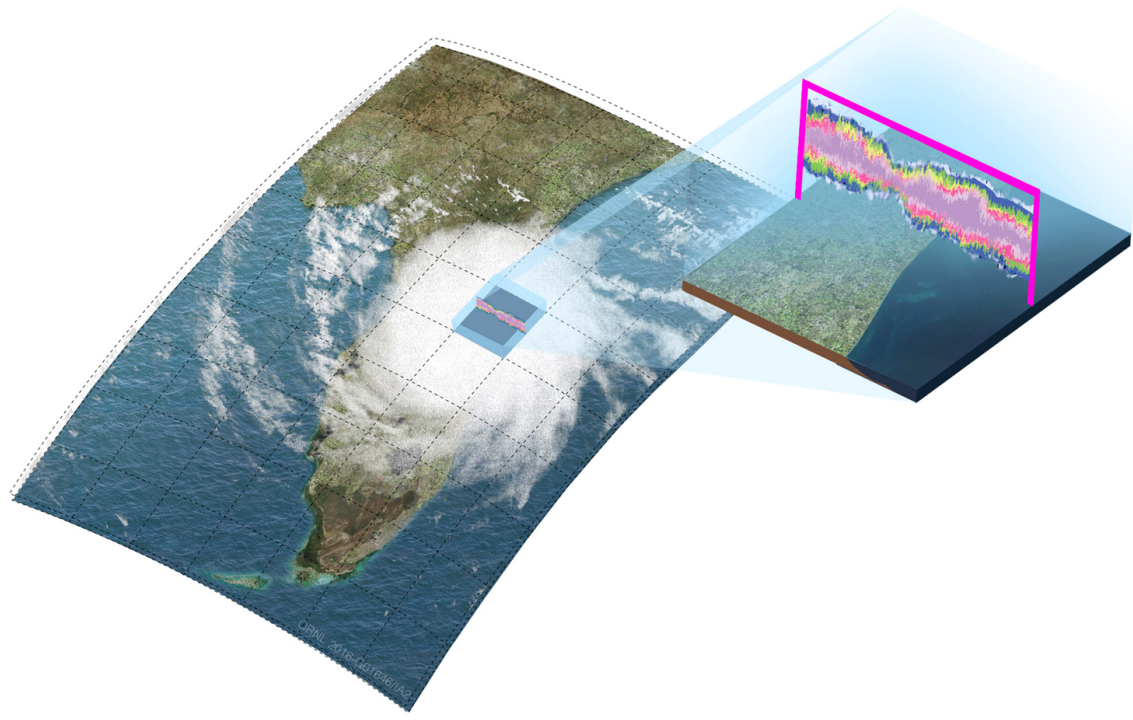


Figure 3.16: Superparametrization by embedding a 2D cloud-resolving model into a 100km model. Figure by Walter Hannah, <http://hannahlab.org/what-is-super-parameterization/>.

### **3.8.4 Machine learning**

Machine learning is increasingly used to replace traditional convective parameterizations in climate and weather models. Traditional convective parameterizations rely on semi-empirical relationships and physical understanding to approximate the effects of unresolved convective motions on the larger scales. In contrast, machine learning techniques attempt to leverage vast amounts of observational and high-resolution simulation data to identify patterns and relationships that govern convection processes.

### **3.8.5 Km-scale models**

Kilometer-scale models of the atmosphere are advanced numerical simulations that focus on the detailed representation of atmospheric processes occurring at scales of around 5 kilometers. These models are increasingly important for capturing the fine-scale features of weather and climate that coarse-resolution models are unable to simulate. Unlike coarser models, kilometer-scale models can explicitly simulate (deep) convection, allowing them to better simulate precipitation, precipitation extremes and the vertical transport of heat and moisture. They serve as the basis for the development of digital twins of Earth.

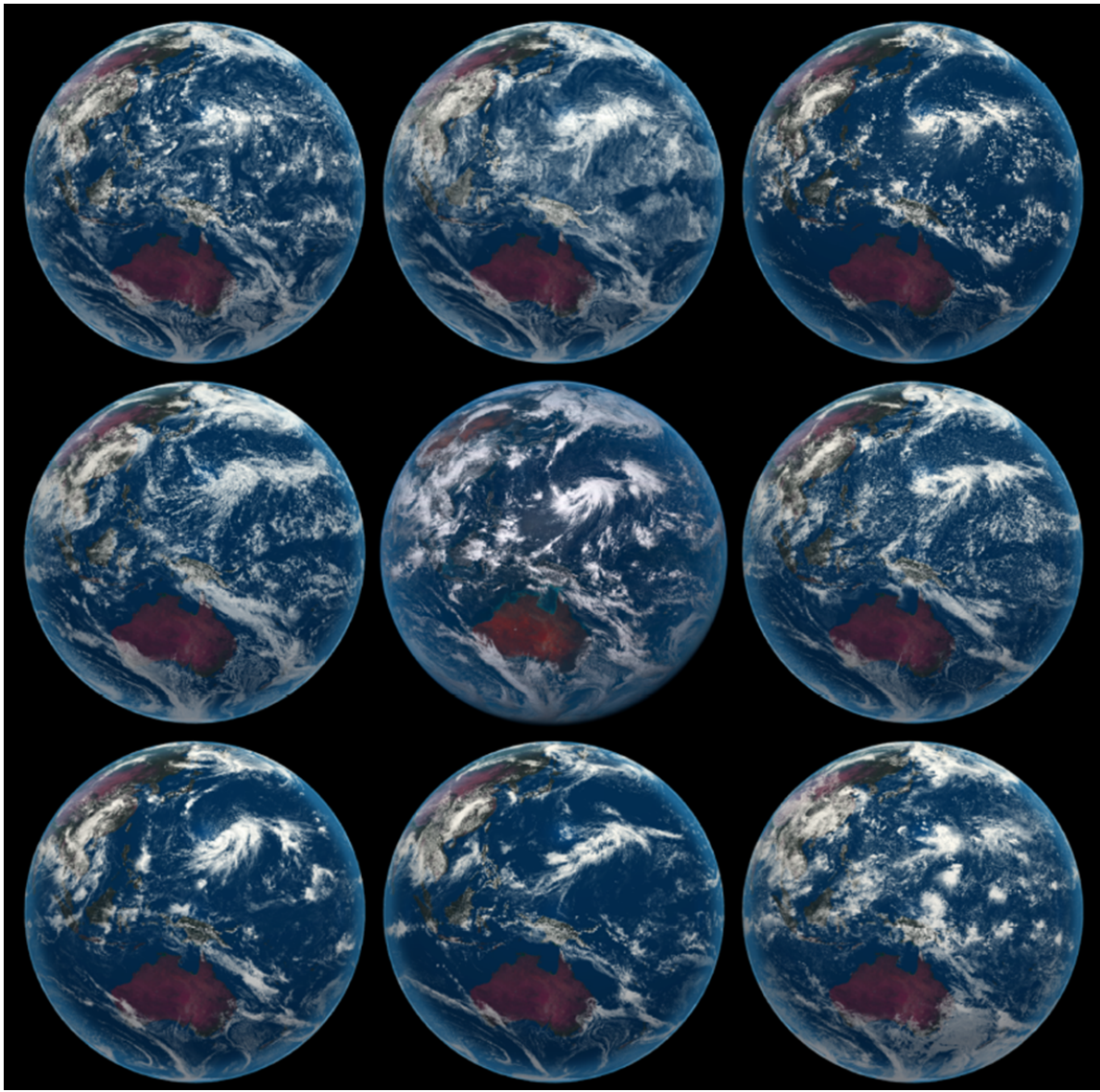


Figure 3.17: Fig. 2 of B. Stevens et al. (2019). The figure shows simulations from 8 km-scale models and compares it to satellite observations in the centre of the plot.

## 4 Interlude: challenges for global km-scale modeling

While kilometer-scale models promise to enhance the simulation of climate and weather, they also present formidable technological challenges. These challenges are briefly discussed in this chapter. Two key challenges are:

- How can we handle the data avalanche generated by global kilometer-scale models?
- Can these models simulate enough days per wall-clock day to be useful?

### 4.1 The data avalanche

The term “data avalanche” refers to the massive amount of data generated by high-resolution climate models. As the spatial resolution of climate simulations is increased down to the kilometer scale, the amount of data produced grows exponentially.

As a concrete example, the ICON-Sapphire model (Hohenegger et al. (2023)) with 5km grid spacing has 20,971,520 grid cells per level and 90 model levels, leading to a total of 1,887,436,800 grid cells. Variables are typically written to output as 32 Bit floating point numbers (8 Byte). Thus, a single timestep of 3-dimensional field like zonal wind, temperature, or cloud liquid water creates an output size of

$$1,887,436,800 \times 4\text{Byte} = 450\text{MByte}.$$

With about 10 3-dimensional fields that one might want to write at least once per day and assuming a simulation length of 10 years, this creates an output of

$$10 \times 10 \times 365 \times 450\text{MByte} = 15\text{TByte}.$$

This simple estimate makes it clear that the output sizes of kilometer-scale models can easily reach the order of petabytes and beyond.

This massive amount of data necessitates solutions for efficient model I/O, mass storage capacities and big data analysis, and it raises the broader question of what data needs to be

stored and which data might be preferable to recompute. Approaches to handle these problems include:

- online and/or object-oriented analysis
- storing data at reduced precision
- employing machine learning (ML) and artificial intelligence (AI) methods for data analysis
- using bit-reproducible codes that enable a checkpoint-recompute-analyze workflow

The checkpoint-recompute-analyze workflow involves saving the state of a simulation at specific intervals (checkpoints) and, if necessary for the scientific analysis, recomputing certain parts of the simulation instead of storing all intermediate data.

A good review of the data avalanche challenge for km-scale modeling is provided by Schär et al. (2020). Figure 4.1 showcases some of the current activities and communities in the area of km-scale modeling.



Figure 4.1: Selected current activities in high-resolution modeling, machine learning and big data for climate and weather. Figure by Aiko Voigt.

## 4.2 Can km-scale models simulate enough days per wall-clock day to be useful?

For climate models to be useful, one usually considers that they should simulated at least 1 day per wall-clock day (1 SYPD = 1 simulated day per wall-clock day). For km-scale models, this can only be achieved by running them on massively-parallel supercomputers with tens

of thousands of compute cores, and it can only be achieved if the models are able to make efficient use of such compute systems.

In this context, the concept of scaling and scalability is crucial <https://hpc-wiki.info/hpc/Scaling>. In the most general sense, scalability is defined as the ability to handle more work as the size of the computer or application grows. Scalability or scaling is widely used to indicate the ability of hardware and software to deliver greater computational power when the amount of resources is increased. For HPC clusters, it is important that they are scalable, in other words the capacity of the whole system can be proportionally increased by adding more hardware. For software, scalability is sometimes referred to as parallelization efficiency — the ratio between the actual speedup and the ideal speedup obtained when using a certain number of processors. In the following, we focus on software scalability and discuss in particular the concepts of speedup and strong scaling.

The speedup in parallel computing can be straightforwardly defined as

$$S = \frac{t(1)}{t(N)},$$

where  $t(1)$  is the computational time for completing a specific task using one processor, and  $t(N)$  is the computational time for completing the same task with  $N$  processors.

In the context of climate modeling, a specific task could be to simulate 1 day. Ideally, we would like climate models to have a linear speedup that is equal to the number of processors ( $S = N$ ), as that would mean that every processor would be contributing 100% of its computational power. Unfortunately, this is a very challenging goal for real world applications to attain.

For strong scaling, the number of processors is increased while the problem size remains constant, i.e., the grid resolution and hence the number of grid cells remains the same. This results in a reduced workload per processor as more and more processors are used.

In October 2024, the lecturer of this class was able to perform strong scaling tests with the ICON-Sapphire model with 5km grid spacing on the Vienna Scientific Cluster VSC5. The task given to the model was to simulate 6 hours and 30 seconds in a prescribed-SST setup in which only the atmospheric model component is used. The scaling was tested for 20, 40, 80, 120 and 140 compute nodes, where each node consists of 128 AMD Zen3 cores. The results are shown in Figure 4.2 and Figure 4.3.

Figure 4.2 shows the time to solution. The gray line shows the situation for perfect strong scaling, as in that case the time to solution for  $N$  nodes or cores would be given by

$$\begin{aligned} t(N) \times N &= t(N = 20) \times 20 \\ t(N) &= t(N = 20) \times \frac{20}{N}, \end{aligned}$$

as an increase in the number of nodes from  $N = 20$  to a higher number  $N$  should decrease the time to solution accordingly. Specifically, for example, when the number of nodes is doubled from 20 to 40, the time to solution should be half.

Figure 4.3 shows the speedup calculated for the same set of simulations.

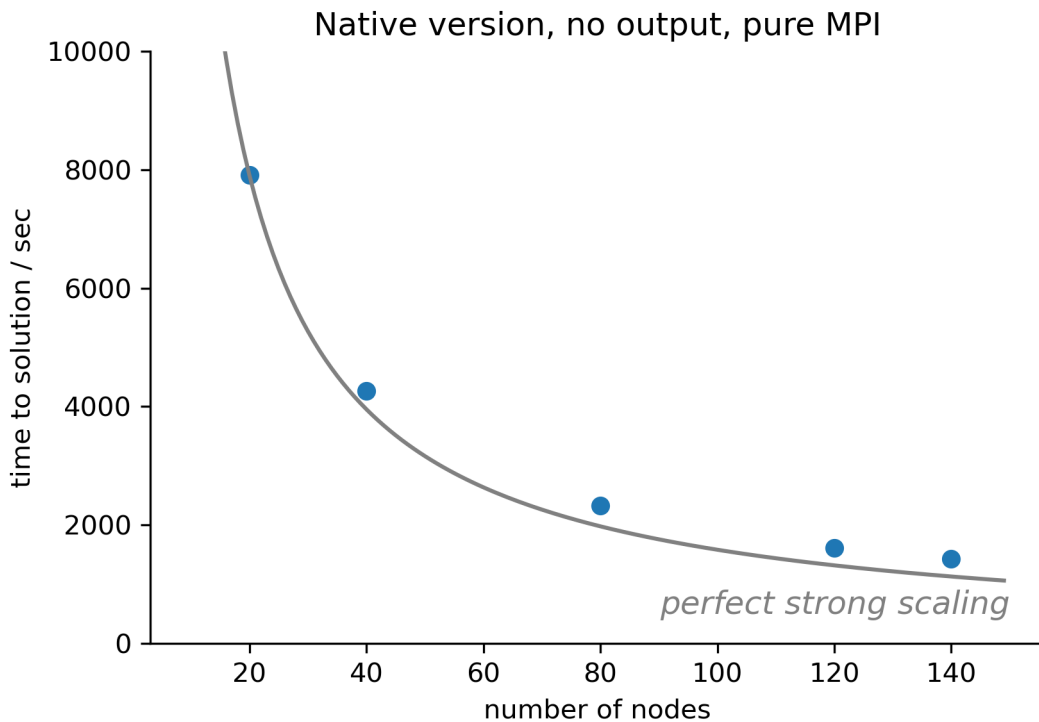


Figure 4.2: ICON-Sapphire strong scaling tests on VSC5 in October 2024. Figure by Aiko Voigt.

Both figures indicate that while the model does not scale perfectly, it shows good strong scaling to at least 140 nodes, i.e., 17,920 cores. The figures also indicate that with 140 nodes, one can expect to achieve

$$\frac{86,400\text{s}}{1,700\text{s}} \times 0.25\text{days} = 12.7\text{days}$$

per wall-clock day, that is 12.7 SDPD. Here, the run time of 1,700s to simulate 6 hours is estimated from Figure 4.2. Assuming perfect strong scaling, 1 SYPD would require about 5,200 nodes. This is larger than the entire VSC5 cluster, which contains 710 nodes, and illustrates that achieving the desired throughput is difficult on pure CPU platforms. As a result CPU/GPU platforms are increasingly used for global km-scale modeling.

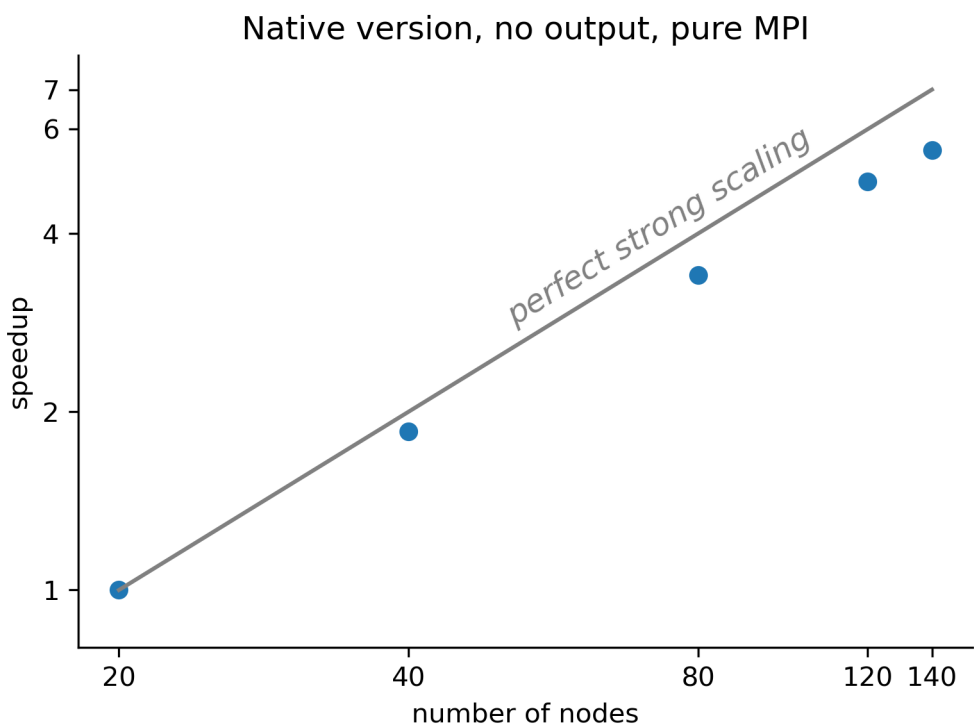


Figure 4.3: ICON-Sapphire strong scaling tests on VSC5 in October 2024. Figure by Aiko Voigt.

# 5 Atmospheric radiation

## 5.1 Planck's law

Planck's law, formulated by Max Planck in 1900, describes the spectral distribution of electromagnetic radiation emitted by a black body in thermal equilibrium at a given temperature. It shows the relationship between the intensity of radiation and the wavelength (or frequency) of the radiation, taking into account both quantum and thermal effects. The law was pivotal in the development of quantum mechanics.

Planck's law can be expressed in terms of wavelength,  $\lambda$ , or frequency,  $\mu$ . For atmospheric radiation, we usually use the wavelength form, which is

$$B_\lambda(T) = \frac{2hc^2}{\lambda^5} \cdot \frac{1}{e^{\frac{hc}{\lambda kT}} - 1}.$$

Here,  $h = 6.626 \cdot 10^{-34}$  Js is Planck's constant,  $c = 3 \cdot 10^8$  m/s is the speed of light,  $k = 1.381 \cdot 10^{-23}$  J/K is the Boltzmann constant,  $T$  is temperature in Kelvin, and  $\lambda$  is wavelength in meters.  $B_\lambda$  has units of  $\text{Wm}^{-2}\text{m}^{-1}\text{sr}^{-1}$ .

## 5.2 Spectral complexity

Figure 5.1 shows the emitted radiation  $B_\lambda$  for different temperatures. The emitted radiation strongly increases with the body's temperature and shifts to shorter and shorter wavelengths (i.e., higher frequencies) as the temperature increases. This behavior as a function of temperature has two fundamental consequences for atmospheric radiation.

1. When  $B_\lambda$  is integrated over one hemisphere and over all wavelengths, one finds the Stefan-Boltzmann law that states that  $F_{BB} = \sigma T^4$ , with  $\sigma = 5.67 \cdot 10^{-8} \text{ Wm}^{-2} \text{ K}^{-4}$ .  $F_{BB}$  is the so-called broadband flux.  $F_{BB}$  has units of  $\text{Wm}^{-2}$ .
2. The sun has a “surface” temperature of around 6000K. Earth's temperature as seen from space is 255K. The strong temperature contrast means that the solar radiation from the sun and the thermal radiation from Earth essentially do not overlap. The two radiative streams can hence be considered in isolation. The solar radiation is often also called shortwave radiation, the thermal radiation is typically also referred to as

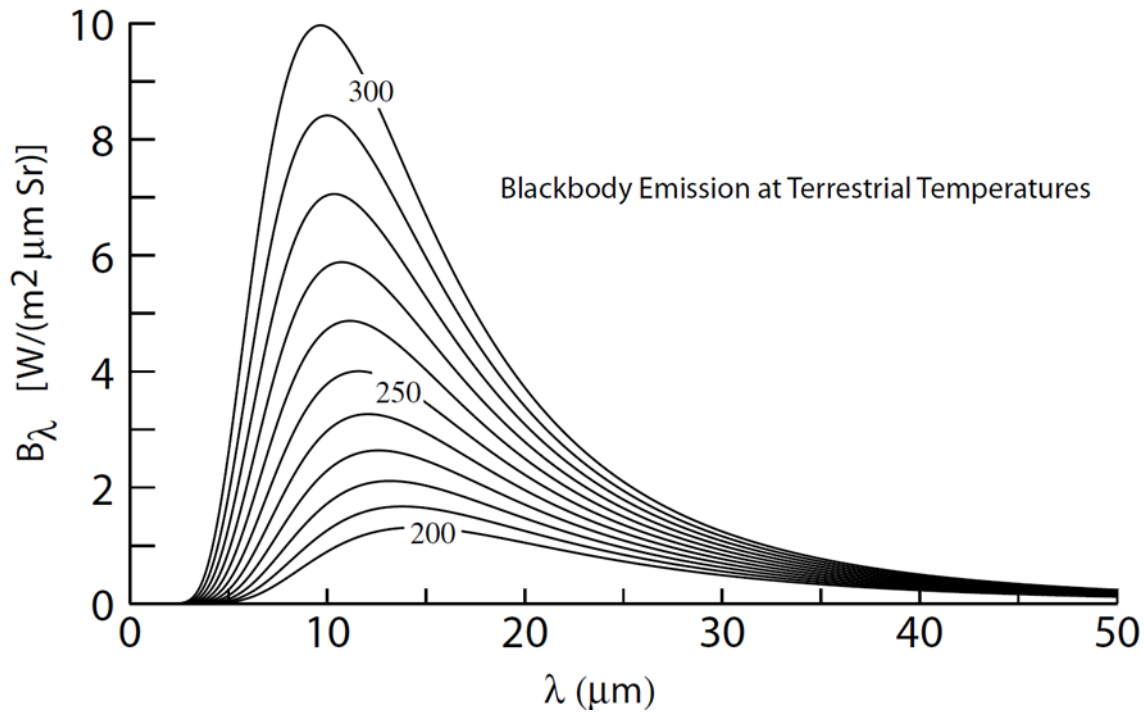


Figure 5.1: Fig. 6.3 of Grant W. Petty (2006).

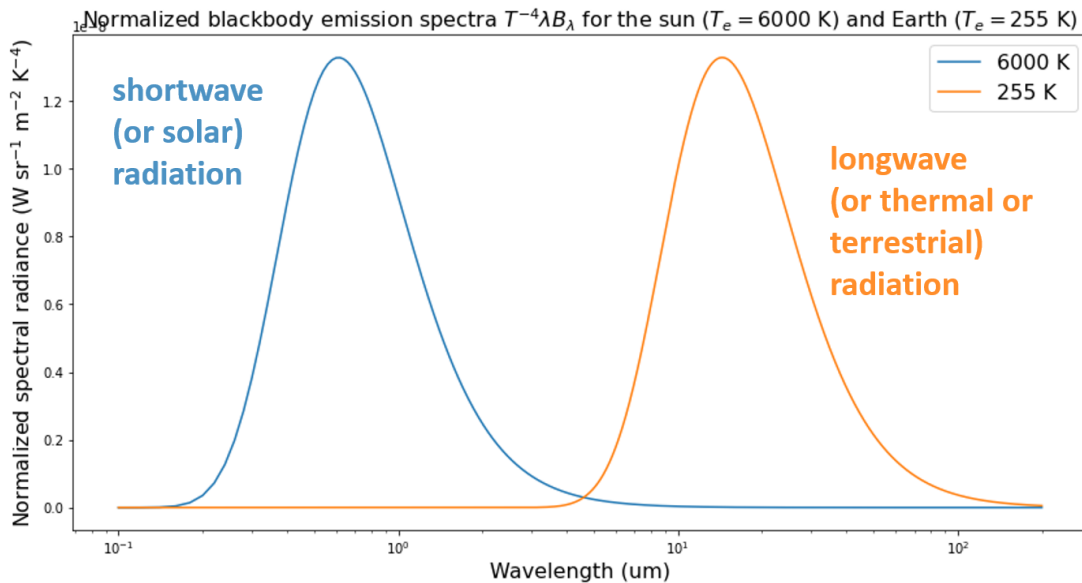


Figure 5.2: Fig. by Brian Rose, SUNY Albany. Taken from <https://brian-rose.github.io/ClimateLaboratoryBook/courseware/radiation.html>. Note that  $B_\lambda$  has been multiplied by  $T \lambda^{-4}$  as otherwise the longwave radiation spectra would not be visible.

longwave radiation. The spectral separation of the two radiation streams is illustrated in Figure 5.2.

The atmosphere scatters and absorbs radiation differently at different wavelengths, and differently between the shortwave and longwave spectral ranges. This is illustrated in Figure 5.3. The figure shows the combined opacity effect of absorption and scattering.

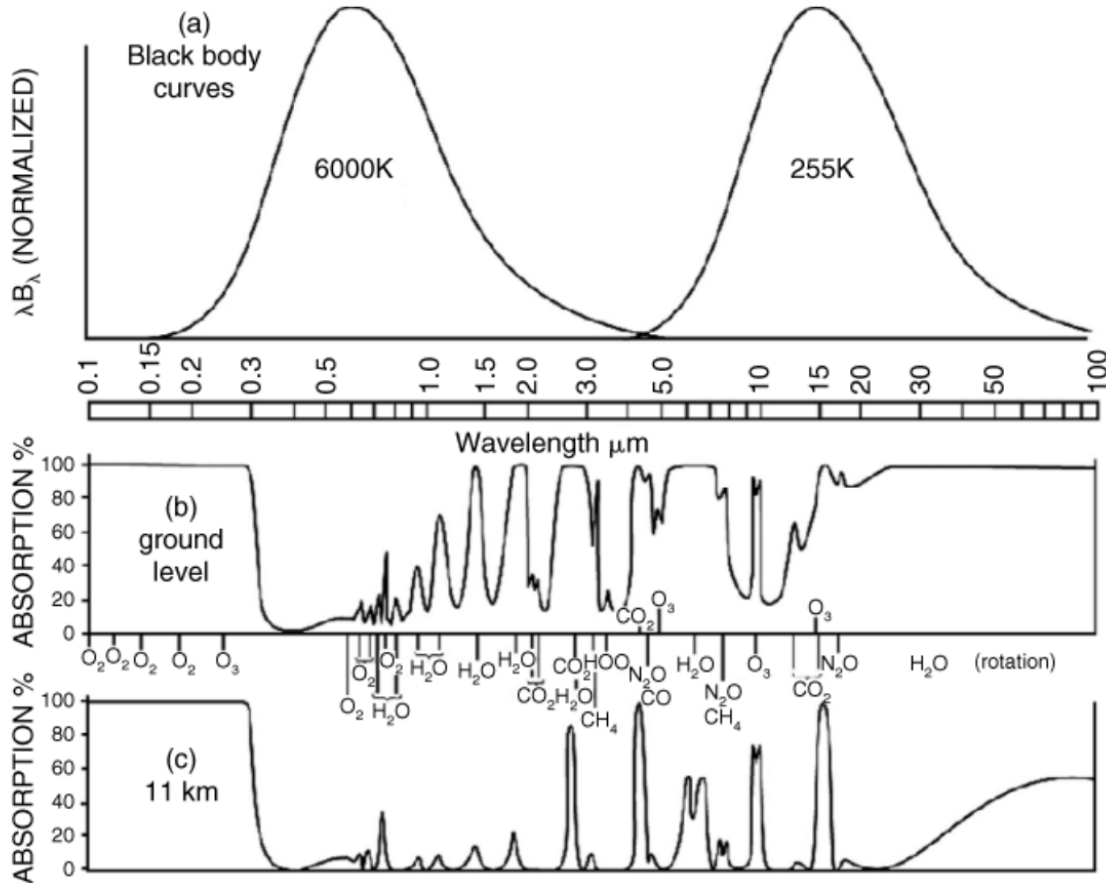


Figure 5.3: (a) The normalized blackbody emission spectra,  $T^{-4} \lambda B_\lambda$  for the Sun ( $T = 6000$  K) and Earth ( $T = 255$  K) as a function of  $\ln \lambda$ . (b) The fraction of radiation absorbed while passing from the ground to the top of the atmosphere as a function of wavelength. (c) The fraction of radiation absorbed from the tropopause (typically at a height of 11 km) to the top of the atmosphere as a function of wavelength. The atmospheric molecules contributing the important absorption features at each frequency are also indicated. Fig. 2.6 of Marshall and Plumb (2008).

- The atmosphere is almost completely transparent in the visible range, right at the peak of the shortwave spectrum.

- The atmosphere is highly opaque in the ultra-violett part of the shortwave spectrum due to ozone and oxygen.
- The opacity at infrared wavelength, defined as wavelengths from  $0.7\mu\text{m}$  to  $1000\mu\text{m}$ , is highly variable.
- Most of the main gases responsible for absorption and scattering are trace gases: H<sub>2</sub>O, CO<sub>2</sub>, CH<sub>4</sub>, N<sub>2</sub>O and O<sub>3</sub>.
- By comparison, the major constituents of the atmosphere are, in decreasing order, 78% N<sub>2</sub>, 21% O<sub>2</sub> and 1% Ar. The major gases are hence nearly completely transparent across the entire spectrum (there are O<sub>2</sub> absorption features in the far UV, but there is little energy at these wavelengths).
- Note that most of the radiatively important gases are tri-atomic molecules. There are fundamental reasons for this: these molecules have modes of rotational and vibration that are easily excited at IR wavelengths. For details, please see the textbook of Grant W. Petty (2006).

The spectral complexity of atmospheric radiation is further illustrated in an animation shown in Figure 5.4. The animation shows the upward longwave radiation as a function of the wavenumber, which is the inverse of wavelength. The animation starts from blackbody radiation at the Earth surface and proceeds to a pressure of 0.1hPa, which can be roughly considered the top of atmosphere. The irradiance at 0.1hPa then corresponds to the outgoing longwave radiation of Earth. The spectral dependence at 0.1hPa is shown in Figure 5.5. An interesting aspect of the animation at low pressure values is that the upward radiation around  $670\text{cm}^{-1}$  increases with height. This is a CO<sub>2</sub> effect - CO<sub>2</sub> in the upper atmosphere cools the atmosphere by emitting more longwave radiation than absorbing it. This cooling of the upper atmosphere is important for stability of atmospheres, as it decreases the kinetic energy of molecules and hence decreases atmospheric escape rates.

[./images/olr-height\\_from-lukas-kluft.mp4](#)

Figure 5.4: Upward spectral longwave radiation as a function of height. Animation by Lukas Kluft, calculated with ARTS line-by-line model.

The animation in Figure 5.6 zooms into the spectrum of upward longwave radiation at 0.1hPa, illustrating the many absorption lines produced by the radiation-relevant gases of the atmosphere. It particular focuses on the wavenumber region around  $670\text{cm}^{-1}$ , where CO<sub>2</sub> absorption is important. A screenshot of the animation is in Figure 5.7.

### 5.3 The atmospheric energy budget and global-mean precipitation

To understand the radiative control of global-mean precipitation, consider the global-mean energy balance of the atmosphere. Let  $E_{atm}$  be the global mean vertically integrated total

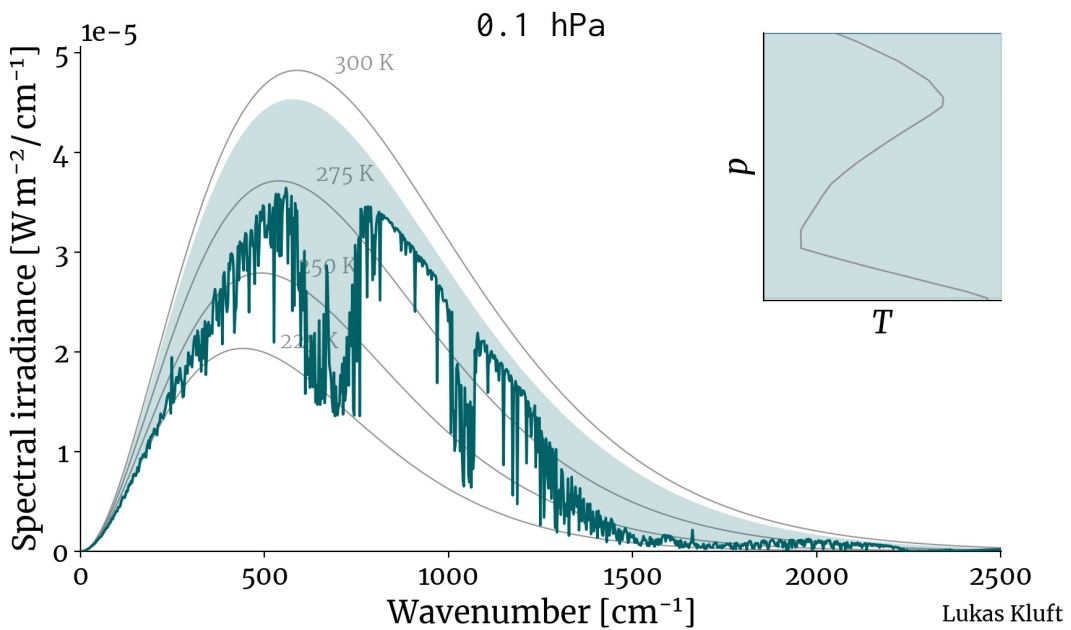


Figure 5.5: Screenshot of the animation in Figure 5.4 at the top-of-atmosphere.

[./images/olr-zoom-fullhd\\_from-lukas-kluft.mp4](#)

Figure 5.6: Zoom into the detailed spectrum of upward longwave radiation at 0.1hPa. Animation by Lukas Kluft, calculated with ARTS line-by-line model.

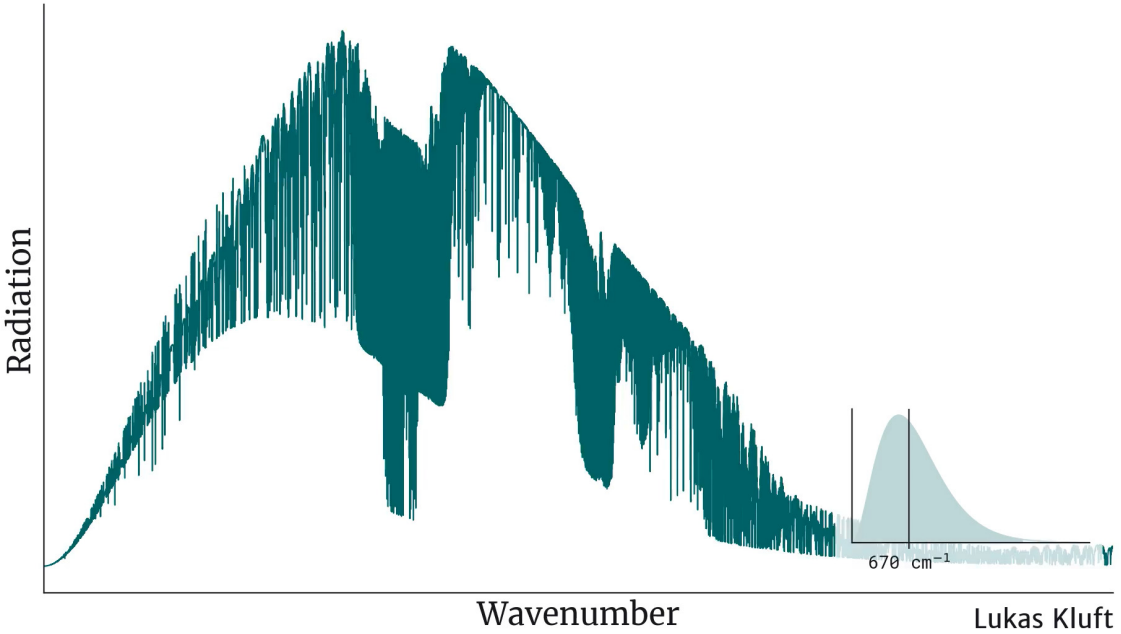


Figure 5.7: Screenshot of the animation in Figure 5.6 at the top-of-atmosphere.

energy of the atmosphere, and let  $F_{TOA}$  and  $F_{SFC}$  be the global-mean energy fluxes at top-of-atmosphere and the surface. Then,

$$\frac{dE_{ATM}}{dt} = F_{TOA} - F_{SFC},$$

with energy fluxes defined as positive downward.

At the top-of-atmosphere, the energy fluxes are purely radiative,

$$F_{TOA} = R_{TOA} = S_{TOA}^\downarrow + S_{TOA}^\uparrow + OLR = (341 - 102 - 239)Wm^{-2} \approx 0Wm^{-2}.$$

$S_{SFC}^{\downarrow, \uparrow}$  are incoming and reflected shortwave radiation, respectively;  $OLR$  is outgoing longwave radiation. The numeric values of the fluxes are taken from Figure 5.8. At the surface,

$$F_{SFC} = R_{SFC} + LH + SH = S_{SFC}^\downarrow + S_{SFC}^\uparrow + L_{SFC}^\downarrow + L_{SFC}^\uparrow + LH + SH.$$

Using again the values from Figure 5.8, one finds

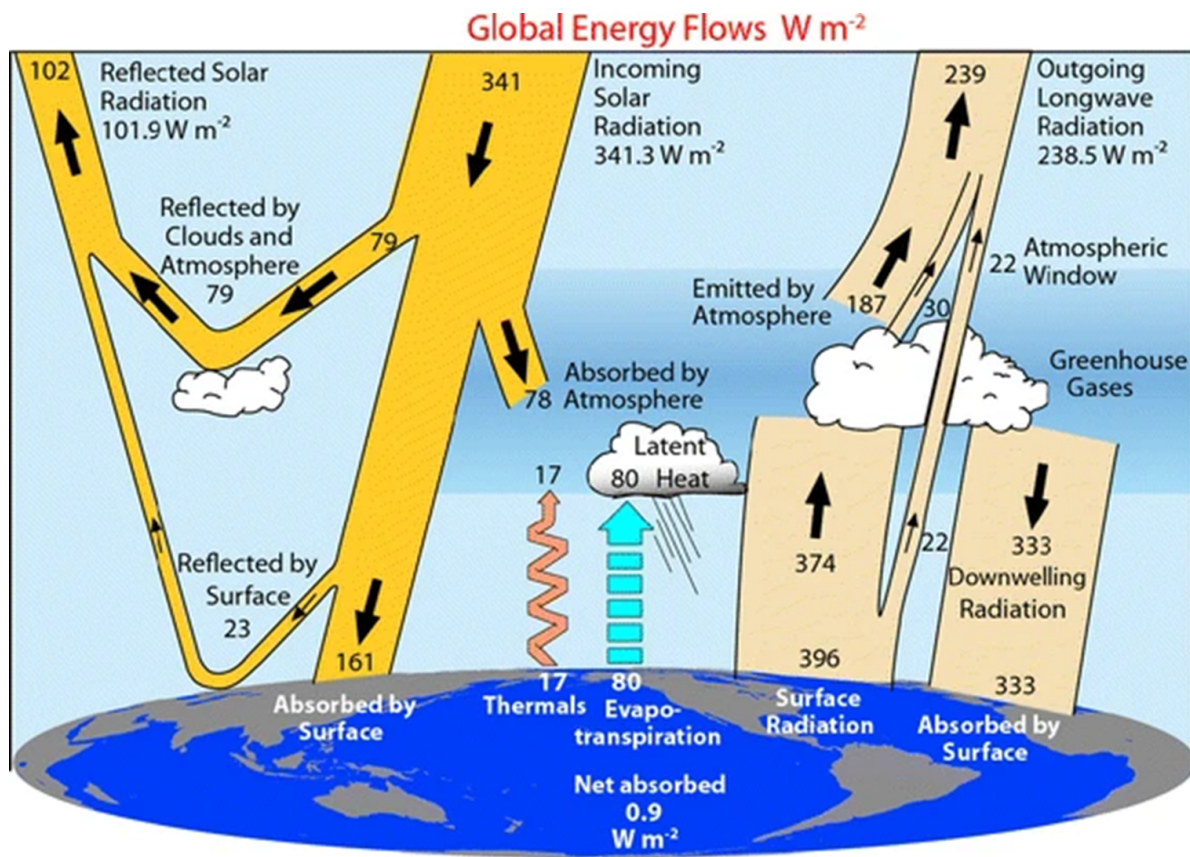


Figure 5.8: Fig. 3.1 of Trenberth (2022)).

$$F_{SFC} = \left( \frac{161}{S_{SFC}^{\downarrow} + S_{SFC}^{\uparrow}} + 333 - 396 - 80 - 17 \right) Wm^{-2} \approx Wm^{-2}.$$

The atmospheric energy balance is then given by

$$\frac{dE_{ATM}}{dt} = F_{TOA} - F_{SFC} = R_{TOA} - R_{SFC} - LH - SH.$$

In equilibrium,  $\frac{dE_{ATM}}{dt} = 0$ , so

$$R_{TOA} - R_{SFC} = R_{ATM} = LH + SHR_{ATM} \approx LH = L_v E = L_v P.$$

The last line uses that in global long-term averages, surface evaporation  $E$  equals surface precipitation  $P$ .  $L_v$  is the latent heat of condensation.

Overall, the above consideration shows that precipitation is strongly linked to atmospheric radiative cooling on the global scale:

- The atmosphere is heated by convection, i.e., mostly the latent heating by condensation of water vapor and a smaller contribution by sensible heating.
- The atmosphere is cooled by the emission of longwave radiation.
- The atmosphere is heated by the absorption of shortwave radiation.
- Because the longwave radiative cooling is larger than the shortwave radiative heating, the net radiative effect is a cooling of the atmosphere.
- Putting aside the smaller sensible heat flux and considering global long-term averages, the net radiative cooling of the atmosphere,  $R_{ATM}$  equals the energy that is put into the atmosphere as a result of surface evaporation,  $L_v E$ , which itself equals  $L_v P$ .
- As a result, radiation controls the global-mean time-mean precipitation that can be produced by the sum of all atmospheric motions, including convective systems.

Note, however, that radiation does not constrain the intensity of individual precipitation events – it only constrains the global sum of all events on long time scales.

An important consequence of the radiative control on global-mean precipitation is that changes in CO<sub>2</sub>, insolation and aerosols lead to two distinct responses in precipitation: a slow and a fast precipitation response. The sum of the two responses is the total precipitation response,

$$dP_{total}/P = dP_{fast}/P + dP_{slow}/P = dP_{fast}/P + \eta dT_s.$$

The fast response depends on the climate forcer (i.e., CO<sub>2</sub>, aerosols, changes in insolation) while the slow response is independent of the climate forcer and scales with the increase in

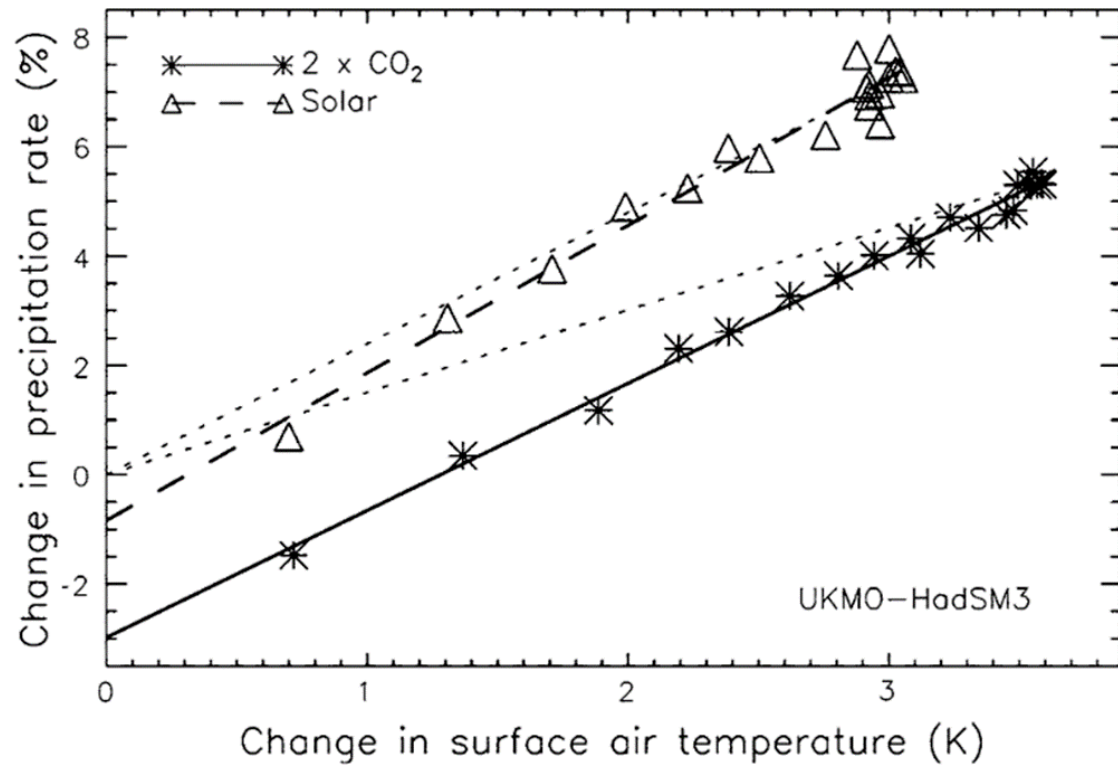


Figure 5.9: Fig. 3 of O'Gorman et al. (2012).

surface temperature according to the so-called hydrological sensitivity  $\eta$ .  $T_s$  is the global-mean surface temperature. A typical value of  $\eta$  is 2-3% per Kelvin of surface warming.

The difference between the fast and slow response is illustrated in Figure 5.9, which compares a simulation in which surface warming is triggered by a doubling of CO<sub>2</sub> with a simulation in which the warming results from an increase in incoming solar radiation at the top of the atmosphere. The hydrological sensitivity, which is estimated as the slope of the regression line, is the same in both simulations. However, the fast response, which is given by the intercept of the regression line with the y-axis, differs: the fast precipitation decline is much stronger for the CO<sub>2</sub> doubling than the increase in solar radiation.

The fact that the fast precipitation response differs for CO<sub>2</sub> and solar radiation implies that even if solar radiation could be decreased to compensate for the warming effect of increased CO<sub>2</sub>, for example through stratospheric aerosol injections, precipitation would still change substantially. This is an important and fundamental limitation of solar geoengineering.

## 5.4 The interplay of radiation and convection in setting the temperature profile of the atmosphere

We now aim to develop some intuition on how radiation and convection interact with each other. To this end, we use the climlab Python package and consider simulations of an atmospheric column subject to radiation and convection. Such a setup is typically referred to as radiative-conductive equilibrium and is what Suki Manabe studied in the 1960s (see the chapter on atmospheric thermodynamics).

The model that we are using combines the RRTM radiative transfer scheme with a hard-conductive adjustment scheme. The details of the implementation are described at <https://brian-rose.github.io/ClimateLaboratoryBook/courseware/rce.html>.

We first consider an isothermal atmosphere. The isothermal atmosphere is stable to convection as can be seen from skew T–ln p diagram in Figure 5.13, yet its temperature profile is not compatible with radiation: the net radiative effect of longwave and shortwave radiation combined is a strong cooling of the atmosphere, except near the surface. The isothermal atmosphere is hence not in equilibrium. When integrating forward in time, we find that convection immediately destroys instability as soon as it is created by radiative cooling. Yet, because radiative cooling is “slow” compared to convection, it takes several weeks for the atmosphere to reach the stable state of radiative-conductive equilibrium. This is shown in the animation in Figure 5.11 and Figure 5.12, which shows the atmospheric state at the end of the simulation.

We now consider an atmosphere in radiative equilibrium. Such an atmosphere is characterized by a very warm surface and very cold troposphere, it is hence unstable to convection, as can be seen from the skew T–ln p diagram in Figure 5.13. When integrated forward in time, convection removes the instability essentially immediately and brings the atmosphere into a

radiative-convective equilibrium. That is, the transition from radiative to radiative-convective equilibrium happens quasi instantaneously. This behavior is shown in the animation in Figure 5.14. As for the case of an isothermal atmosphere, the final state is the same state of radiative-convective equilibrium shown in Figure 5.12.

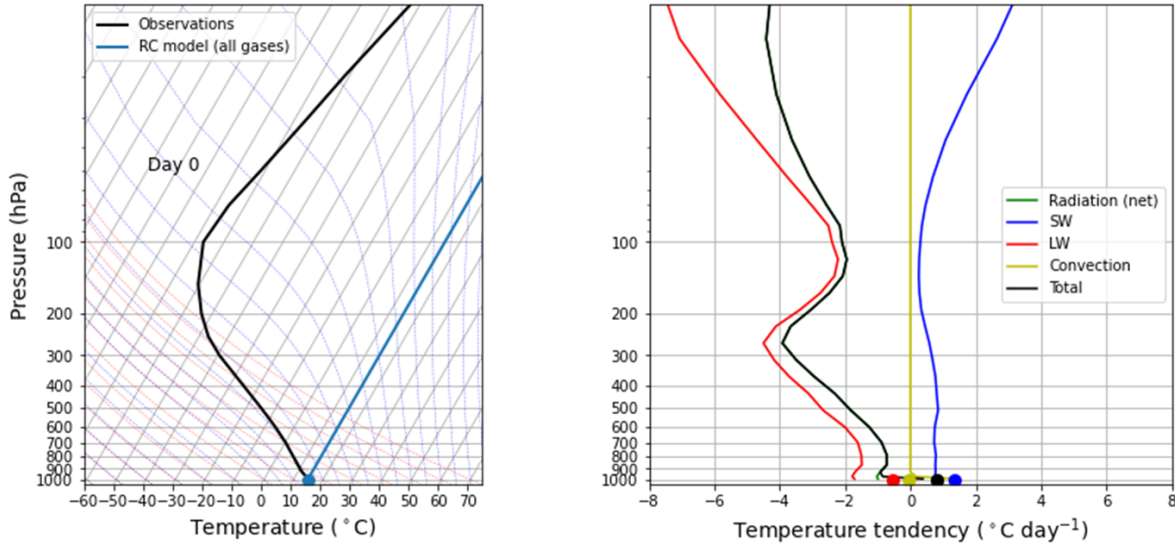


Figure 5.10: Isothermal atmosphere. Left: temperature structure in a skew  $T - \ln p$  diagram. Right: heating rates from convection, longwave and shortwave radiation. Taken from <https://brian-rose.github.io/ClimateLaboratoryBook/courseware/rce.html>.

[./images/rose\\_climlab\\_rce\\_adjustment-from-isothermal-atmosphere.mp4](#)

Figure 5.11: Taken from <https://brian-rose.github.io/ClimateLaboratoryBook/courseware/rce.html>. Animation by Brian Rose of SUNY Albany, calculated with climlab Python package.

Overall, these considerations show that while radiation cools the atmosphere (or more precisely the troposphere), convection heats it. Because radiative cooling creates the need for convection, the magnitude of radiative cooling controls the amount of convective heating and, as discussed above, the amount of time-mean global-mean precipitation.

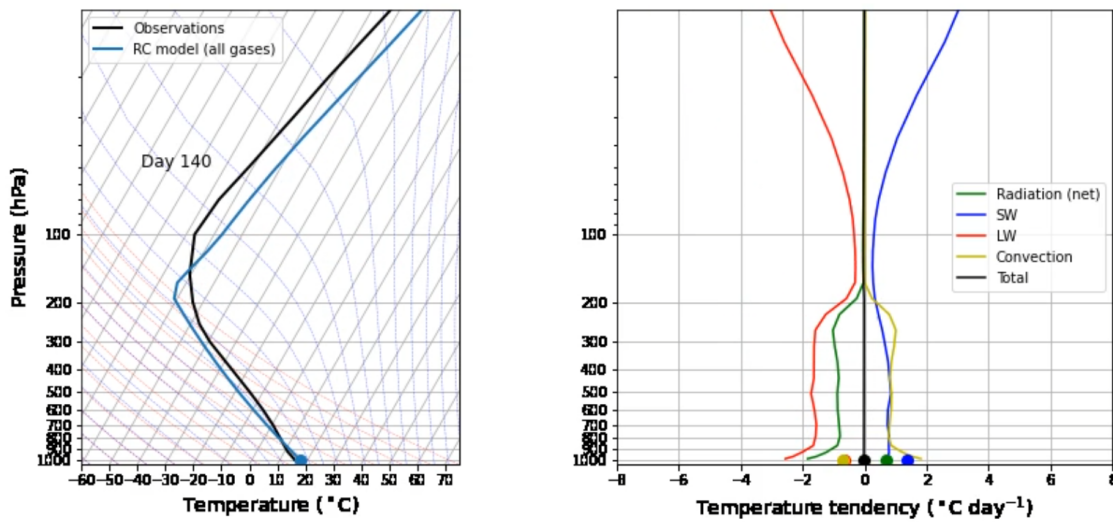


Figure 5.12: Radiative-convective equilibrium reached after starting from the isothermal atmosphere in Figure 5.13.

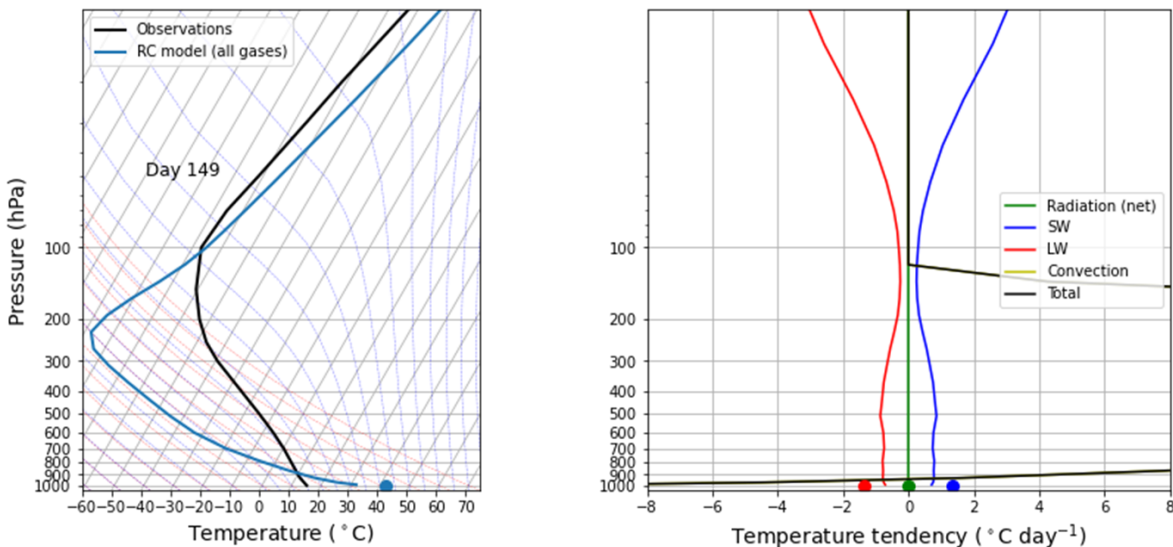


Figure 5.13: As in Figure 5.13 but for an atmosphere in radiative equilibrium.

[./images/rose\\_climlab\\_rce\\_adjustment-from-radequilibrium-atmosphere.mp4](#)

Figure 5.14: Taken from <https://brian-rose.github.io/ClimateLaboratoryBook/courseware/rce.html>. Animation by Brian Rose of SUNY Albany, calculated with climlab Python package.

## 5.5 Representation of radiation in climate and weather models

The general form of the radiative transfer equation is the Schwarzschild equation, which accounts for both scattering and absorption/emission effects along a path in a medium. It is given by:

$$\frac{dI(\hat{\Omega})}{d\tau} = -I(\hat{\Omega}) + (1 - \tilde{\omega})B_\lambda + \frac{\tilde{\omega}}{4\pi} \int_{4\pi} p(\hat{\Omega}', \hat{\Omega})I(\hat{\Omega}')d\omega'.$$

Here,  $I$  is the radiance in units of  $\text{Wm}^{-2}\text{m}^{-1}\text{sr}^{-1}$ ,  $\tau$  is the optical depth given by  $d\tau = \beta_e s$  with  $\beta_e$  being the extinction coefficient in  $\text{m}^{-1}$  and  $s$  being the geometric path length, and  $\hat{\Omega}$  is the angle of the direction of the radiance. On the r.h.s.,  $\tilde{\omega}$  is the single scattering albedo, given by the ratio of the scattering coefficient  $\beta_s$  and  $\beta_e$ .  $B_\lambda$  is the Planck function,  $p$  is the scattering phase function and  $\omega'$  is a solid angle.

On the r.h.s., the first term is the extinction by absorption and scattering out of beam direction  $\hat{\Omega}$ . This term is a sink term. The other two terms are source terms and describe the emission and scattering from other directions into the beam direction. The single scattering albedo control the weight given to each of the two source terms. If  $\tilde{\omega} = 0$ , the scattering term is zero. This is a good approximation for longwave radiation. If  $\tilde{\omega} = 1$ , the thermal emission vanishes. This is a good approximation for shortwave radiation.

The radiative transfer equation is an integrodifferential equation. Thus, in order to determine the radiance  $I$  at a given value of the optical depth and beam direction, we must simultaneously determine  $I$  for all values of optical depth and beam directions. This makes radiation a hard problem to solve, although the underlying physics are well understood. Different from the problem of parametrizing convection, the problem is not in a lack of physical understanding of the phenomena but in the computational cost to compute it.

To make radiation tractable in models, several approaches are combined:

- Longwave and shortwave radiation are treated separately.
- The 2-stream approximation simplifies the radiative transfer equations into one stream of upward radiative flux and one stream of downward radiative flux.
- The k-distribution method allows for a more efficient integration over frequencies in a given spectral band by reordering frequencies according to the absorption coefficient.
- Detailed descriptions and derivations of both methods are given in, e.g., Grant W. Petty (2006).
- Radiation is called less frequently than other parts of the models.

Even with these approaches, radiation is one of the most, if not the most computationally expensive part of weather and climate models. A testimony for this is given in Figure 5.15, Figure 5.16 and Figure 5.17 show screenshots from a simulation with the global ICON climate model run with a horizontal resolution of around 160km (R2B4), 47 levels and a time step of

15 minutes. Radiation, however, is called only every 1.5 hours. The model was run on the Vienna Scientific Cluster VSC4 using 3 nodes with a total of 144 compute cores and pure MPI parallelization. Simulating 5 years in this setup took 4 hours and 30 minutes of wall clock time.

Less than half of the total time is spent in the dynamical core of the model: around 6,400s are used to complete the routine “nh\_solve”. About 1,000s are spent by converting fields from the dynamical core to the physics of the model and back; this is given by the routines “dyn2phy” and “phy2dyn”. Most of the rest of the calculation is spent in the physics of the model (“echam\_phy”), which are themselves dominated by the calculation of radiation (“radiation”). Infact, the calculation of radiation alone requires about 4,000s, which is almost 25% of the entire computation. This is despite the fact that radiation is called only every 6th time step. If it was called every time step, its cost would increase to 24,000s and the overall simulation time would more than double from 16,000s to 36,000s!

```

340   /
341   &echam_phy_nml
342     ! domain 1
343     ! atmospheric physics ("" = never)
344     echam_phy_config(1)%dt_rad = 'PT90M'
345     echam_phy_config(1)%dt_vdf = 'PT15M'
346     echam_phy_config(1)%dt_cnv = 'PT15M'
347     echam_phy_config(1)%dt_cld = 'PT15M'
348     echam_phy_config(1)%dt_gwd = 'PT15M'
349     echam_phy_config(1)%dt_sso = 'PT15M'
350     ! atmospheric chemistry ("" = never)
351     echam_phy_config(1)%dt_mox = 'PT15M'
352     ! surface (true or false)
353     echam_phy_config(1)%ljsb = .true.
354     echam_phy_config(1)%lamip = .true.
355     echam_phy_config(1)%lice = .true.
356     echam_phy_config(1)%lmlo = .false.
357     echam_phy_config(1)%llake = .true.
358   /
359   &echam_rad_nml

```

Figure 5.15: Part of the namelist of the ICON simulation. The part specifies the time intervals at which the parametrizations of the model are called. While most parametrizations are called every 15 minutes, radiation is called only every 1.5 hours. This is 6 times less often. Simulation by Aiko Voigt.

3257954	Timer report, ranks 0-143										
	name	# calls	t_min	min rank	t_avg	t_max	max rank	total min (s)	total min rank	total max (s)	total max rank
3257955	<b>total</b>	144	04h31m	[48]	04h31m	04h31m	[121]	16271.286	[48]	16271.254	[121]
3257956	L <b>integrate_nh</b>	25242624	0.06296s	[9]	0.09112s	1.2424s	[62]	15950.270	[107]	16002.172	[43]
3257957	L <b>nh_solve</b>	201940992	0.00352s	[97]	0.00446s	0.11300s	[2]	6094.235	[23]	6487.079	[120]
3257958	L <b>nh_hdiff</b>	25242768	0.00055s	[7]	0.00070s	0.00574s	[84]	115.777	[70]	132.567	[23]
3257959	L <b>transport</b>	25242624	0.00373s	[106]	0.00476s	0.01028s	[113]	821.808	[36]	847.426	[18]
3257960	L <b>iconam_echam</b>	25242624	0.02120s	[18]	0.04749s	1.1923s	[85]	8172.796	[10]	8471.777	[43]
3257961	L <b>dyn2phy</b>	25242624	0.00193s	[69]	0.00241s	0.00481s	[110]	486.183	[87]	481.741	[27]
3257962	L <b>d2p_prep</b>	75727872	0.00005s	[33]	0.00021s	0.00206s	[84]	108.516	[104]	121.034	[71]
3257963	L <b>d2p_sync</b>	50485248	0.00004s	[75]	0.00010s	0.00261s	[40]	27.118	[123]	43.741	[45]
3257964	L <b>d2p_couple</b>	25242624	0.00121s	[60]	0.00157s	0.00328s	[73]	261.585	[87]	335.098	[27]
3257965	L <b>echam_bcs</b>	25242624	0.00005s	[27]	0.00010s	1.0099s	[36]	15.509	[27]	19.889	[87]
3257966	L <b>echam_phy</b>	25242624	0.01562s	[99]	0.04100s	0.28903s	[70]	6967.535	[99]	7462.136	[48]
3257967	L <b>interface_echam_cov</b>	227183616	0.00002s	[90]	0.00002s	0.00136s	[1]	36.173	[14]	41.070	[37]
3257968	L <b>interface_echam_rht</b>	227183616	0.00000s	[5]	0.00001s	0.00061s	[7]	13.113	[27]	23.228	[0]
3257969	L <b>interface_echam_vdf</b>	227183616	0.00008s	[77]	0.00122s	0.00992s	[112]	1847.876	[57]	2001.571	[120]
3257970	L <b>vdiff_down</b>	227183616	0.00015s	[4]	0.00019s	0.00265s	[105]	291.460	[57]	307.578	[133]
3257971	L <b>update_surface</b>	227183616	0.00074s	[134]	0.00094s	0.00963s	[112]	1418.550	[57]	1546.347	[120]
3257972	L <b>ice_fast</b>	227183616	0.00000s	[0]	0.00000s	0.00059s	[138]	0.847	[51]	1.380	[120]
3257973	L <b>jacob</b>	227183616	0.00073s	[77]	0.00092s	0.00960s	[112]	1389.373	[57]	1511.957	[120]

Figure 5.16: Summary of time spent in different parts of the simulation - Part 1. Simulation by Aiko Voigt.

3257998		L ice_fast	227183616	0.00000s [0]	0.00000s	0.00059s [138]	0.847 [51]	1.380 [128]
3257999		L jsbach	227183616	0.000073s [77]	0.00002s	0.00060s [112]	1389.373 [57]	1511.957 [128]
3258000		L vdiff_up	227183616	0.00003s [128]	0.00004s	0.00113s [11]	57.559 [57]	64.082 [12]
3258001		L interface_echam_gad	227183616	0.00025s [33]	0.00027s	0.00190s [88]	425.051 [77]	446.770 [8]
3258002		L interface_echam_sso	227183616	0.00001s [1]	0.00004s	0.00137s [101]	16.223 [27]	151.141 [122]
3258003		L interface_echam_cnv	227183616	0.00011s [113]	0.00016s	0.00279s [116]	199.457 [111]	300.534 [107]
3258004		L interface_echam_cld	227183616	0.00007s [2]	0.00011s	0.00360s [1]	128.061 [14]	212.450 [8]
3258005		L interface_echam_mox	227183616	0.00001s [2]	0.00002s	0.00134s [113]	24.408 [109]	30.943 [8]
3258006		L interface_echam_wmo	227183616	0.00001s [2]	0.00002s	0.00092s [121]	25.165 [41]	27.138 [27]
3258007		L radiation	25242624	0.00000s [0]	0.02383s	0.25965s [70]	4040.122 [111]	4390.103 [110]
3258008		L lrtm	37863936	0.00449s [6]	0.00579s	0.01126s [128]	1463.54s [68]	1745.822 [110]
3258009		L srtm	37863936	0.00409s [137]	0.00569s	0.01212s [78]	1422.791 [111]	1566.162 [142]
3258010		L phy2dyn	25242624	0.00167s [129]	0.00395s	0.13678s [111]	382.859 [48]	988.334 [68]
3258011		L p2d_prep	50485248	0.00005s [2]	0.00007s	0.00127s [23]	22.785 [99]	35.087 [119]
3258012		L p2d_sync	50485248	0.00005s [59]	0.00130s	0.13033s [111]	141.948 [8]	755.447 [68]
3258013		L p2d_couple	25242624	0.00110s [109]	0.00122s	0.00364s [77]	207.982 [59]	221.893 [30]
3258014		L nesting	25242624	0.00000s [0]	0.00000s	0.00051s [113]	0.057 [6]	0.103 [52]
3258015		L exch_data	1313202240	0.00000s [18]	0.00020s	0.13033s [111]	1249.527 [0]	2332.211 [75]
3258016		L exch_data.wait	1313202240	0.00000s [0]	0.00010s	0.13028s [111]	204.911 [71]	1653.310 [75]
3258017		global_sum	144	0.00004s [76]	0.00074s	0.00132s [58]	0.000 [76]	0.001 [58]
3258018		ordglb_sum	2880	0.00000s [96]	0.00003s	0.00039s [0]	0.001 [19]	0.001 [94]
3258019		wrt_output	8784	0.12319s [0]	0.14828s	0.22463s [122]	9.026 [0]	9.066 [82]
3258020		nh_diagnostics	25243488	0.00044s [82]	0.00063s	0.00473s [2]	100.458 [3]	122.836 [123]
3258021		.....						

Figure 5.17: Summary of time spent in different parts of the simulation - Part 2. Simulation by Aiko Voigt.

# References

- Akmaev, R. A. 1991. "A Direct Algorithm for Convective Adjustment of the Vertical Temperature Profile for an Arbitrary Critical Lapse Rate." *Mon. Wea. Rev.* 119 (10): 2499–2504. [https://doi.org/10.1175/1520-0493\(1991\)119%3C2499:ADAFCA%3E2.0.CO;2](https://doi.org/10.1175/1520-0493(1991)119%3C2499:ADAFCA%3E2.0.CO;2).
- Brönnimann, Stefan. 2018. *Klimatologie*. UTB GmbH.
- Hill, Spencer A., Yi Ming, Isaac M. Held, and Ming Zhao. 2017. "A Moist Static Energy Budget-Based Analysis of the Sahel Rainfall Response to Uniform Oceanic Warming." *J. Climate* 30 (15): 5637–60. <https://doi.org/10.1175/JCLI-D-16-0785.1>.
- Hohenegger, C., P. Korn, L. Linardakis, R. Redler, R. Schnur, P. Adamidis, J. Bao, et al. 2023. "ICON-Sapphire: simulating the components of the Earth system and their interactions at kilometer and subkilometer scales." *Geosci. Model Dev.* 16 (2): 779–811. <https://doi.org/10.5194/gmd-16-779-2023>.
- Kluft, Lukas, Sally Dacie, Stefan A. Buehler, Hauke Schmidt, and Bjorn Stevens. 2019. "Re-Examining the First Climate Models: Climate Sensitivity of a Modern Radiative–Convective Equilibrium Model." *J. Climate* 32 (23): 8111–25. <https://doi.org/10.1175/JCLI-D-18-0774.1>.
- Lohmann, Ulrike, Felix Lüönd, and Fabian Mahrt. 2016. *An Introduction to Clouds: From the Microscale to Climate*. Cambridge University Press.
- Maher, Penelope, Edwin P. Gerber, Brian Medeiros, Timothy M. Merlis, Steven Sherwood, Aditi Sheshadri, Adam H. Sobel, Geoffrey K. Vallis, Aiko Voigt, and Pablo Zurita-Gotor. 2019. "Model Hierarchies for Understanding Atmospheric Circulation." *Rev. Geophys.* 57 (2): 250–80. <https://doi.org/10.1029/2018RG000607>.
- Manabe, S., and R. F. Strickler. 1964. "Thermal equilibrium of the atmosphere with a convective adjustment." *J. Atmos. Sci.* 21 (4): 361–85.
- Marshall, John, and R. Alan Plumb. 2008. *Atmosphere, Ocean, and Climate Dynamics*. Elsevier.
- Möbis, B., and B. Stevens. 2012. "Factors controlling the position of the ITCZ on an Aquaplanet." *J. Adv. Model. Earth Syst.* 4: M00A04. <https://doi.org/10.1029/2012MS000199>.
- O'Gorman, Paul A., Richard P. Allan, Michael P. Byrne, and Michael Previdi. 2012. "Energetic Constraints on Precipitation Under Climate Change." *Surveys in Geophysics* 33 (3): 585–608. <https://doi.org/10.1007/s10712-011-9159-6>.
- Petty, G. W. 2008. *A First Course in Atmospheric Thermodynamics*. Sundog Publishing.
- Petty, Grant W. 2006. *A First Course in Atmospheric Radiation*. Sundog Publishing.
- Schär, Christoph, Oliver Fuhrer, Andrea Arteaga, Nikolina Ban, Christophe Charpiloz, Salvatore Di Girolamo, Laureline Hentgen, et al. 2020. "Kilometer-Scale Climate Models:

- Prospects and Challenges.” *Bull. Amer. Meteor. Soc.* 101 (5): E567–87. <https://doi.org/10.1175/BAMS-D-18-0167.1>.
- Siebesma, A. P., S. Bony, C. Jakob, and B. Stevens, eds. 2020. *Clouds and Climate: Climate Science’s Greatest Challenge*. Cambridge University Press. <https://doi.org/10.1017/9781107447738>.
- Stensrud, David J. 2007. “Parameterization Schemes: Keys to Understanding Numerical Weather Prediction Models.” In *Parameterization Schemes*. United States: Cambridge University Press.
- Stevens, Bjorn, Claudia Acquistapace, Akio Hansen, Rieke Heinze, Carolin Klinger, Daniel Klocke, Harald Rybka, et al. 2020. “The Added Value of Large-Eddy and Storm-Resolving Models for Simulating Clouds and Precipitation.” *J. Meteorol. Soc. Japan* 98 (2): 395–435. <https://doi.org/10.2151/jmsj.2020-021>.
- Stevens, B., M. Satoh, L. Auger, J. Biercamp, C. S. Bretherton, X. Chen, P. Düben, et al. 2019. “DYAMOND: the DYnamics of the Atmospheric general circulation Modeled On Non-hydrostatic Domains.” *Prog. Earth Planet Sci.* 6 (61). <https://doi.org/10.1186/s40645-019-0304-z>.
- Trenberth, Kevin E. 2022. *The Changing Flow of Energy Through the Climate System*. Cambridge University Press. <https://doi.org/10.1017/9781108979030>.
- Wallace, J. M., and P. V. Hobbs. 2006. *Atmospheric Science: An Introductory Survey*. International Geophysics Series. Elsevier Academic Press.